

DEACTIVATION OF MANGANESE DIOXIDE ELECTROCATALYST IN ZINC-AIR BATTERIES
STUDIED VIA DENSITY FUNCTIONAL THEORY



A Thesis Submitted in Partial Fulfillment of the Requirements
for the Degree of Master of Engineering in Chemical Engineering

Department of Chemical Engineering

FACULTY OF ENGINEERING

Chulalongkorn University

Academic Year 2020

Copyright of Chulalongkorn University



จุฬาลงกรณ์มหาวิทยาลัย
CHULALONGKORN UNIVERSITY

การเสื่อมสภาพของตัวเร่งปฏิกิริยาแมงกานีสไดออกไซด์ในแบตเตอรี่สังกะสี-อากาศศึกษาโดยทฤษฎี
ฟังก์ชันนอลความหนาแน่น



วิทยานิพนธ์นี้เป็นส่วนหนึ่งของการศึกษาตามหลักสูตรปริญญาวิศวกรรมศาสตรมหาบัณฑิต
สาขาวิชาวิศวกรรมเคมี ภาควิชาวิศวกรรมเคมี
คณะวิศวกรรมศาสตร์ จุฬาลงกรณ์มหาวิทยาลัย
ปีการศึกษา 2563
ลิขสิทธิ์ของจุฬาลงกรณ์มหาวิทยาลัย

Thesis Title DEACTIVATION OF MANGANESE DIOXIDE
ELECTROCATALYST IN ZINC-AIR BATTERIES STUDIED VIA
DENSITY FUNCTIONAL THEORY

By Mr. Puwit Buapin

Field of Study Chemical Engineering

Thesis Advisor Assistant Professor SUPAREAK PRASERTHDAM, Ph.D.

Thesis Co Advisor Associate Professor SOORATHEP KHEAWHOM, Ph.D.
Meena Rittiruum, Ph.D.

Accepted by the FACULTY OF ENGINEERING, Chulalongkorn University in
Partial Fulfillment of the Requirement for the Master of Engineering

..... Dean of the FACULTY OF
ENGINEERING
(Professor SUPOT TEACHAVORASINSKUN, D.Eng.)

THESIS COMMITTEE

..... Chairman
(Professor SARAWUT RIMDUSIT, Ph.D.)

..... Thesis Advisor
(Assistant Professor SUPAREAK PRASERTHDAM, Ph.D.)

..... Thesis Co-Advisor
(Associate Professor SOORATHEP KHEAWHOM, Ph.D.)

..... Thesis Co-Advisor
(Meena Rittiruum, Ph.D.)

..... Examiner
(Professor JOONGJAI PANPRANOT, Ph.D.)

..... Examiner
(MANASWEE SUTTIPONG, Ph.D.)

..... External Examiner
(Associate Professor Pornjuk Srepusharawoot, Ph.D.)

ภูวิศ บัวผิน : การเสื่อมสภาพของตัวเร่งปฏิกิริยาแมงกานีสไดออกไซด์ในแบตเตอรี่
 สังกะสี-อากาศศึกษาโดยทฤษฎีฟังก์ชันนอลความหนาแน่น. (DEACTIVATION OF
 MANGANESE DIOXIDE ELECTROCATALYST IN ZINC-AIR BATTERIES STUDIED
 VIA DENSITY FUNCTIONAL THEORY) อ.ที่ปรึกษาหลัก : ผศ. ดร.ศุภฤกษ์ ประเสริฐ
 ธรรม, อ.ที่ปรึกษาร่วม : รศ. ดร.สุรเทพ เขียวหอม,ดร.มีนา ฤทธิร่วม

แมงกานีสไดออกไซด์เป็นตัวเร่งปฏิกิริยาเชิงไฟฟ้าที่ใช้ในขั้วแคโทดของแบตเตอรี่สังกะสี-
 อากาศที่มีปฏิกิริยารีดักชันของออกซิเจน มีงานวิจัยมากมายที่ศึกษาเกี่ยวกับประสิทธิภาพของ
 ปฏิกิริยารีดักชันของออกซิเจนมากกว่างานวิจัยที่ศึกษาถึงการเสื่อมสภาพของของตัวเร่ง
 ปฏิกิริยา โดยงานวิจัยนี้ได้ศึกษาการเสื่อมสภาพของตัวเร่งปฏิกิริยาแมงกานีสไดออกไซด์ใน
 เฟสอัลฟาและเบต้าผ่านทฤษฎีฟังก์ชันนอลความหนาแน่น สำหรับผลของการเปลี่ยนเฟสจากอัลฟา
 211 ไปเป็นเบต้า 110 บนแมงกานีสไดออกไซด์นั้น ทำให้เกิดการเสื่อมสภาพของตัวเร่งปฏิกิริยา
 เพราะค่าความต่างศักย์เกินของเฟสเบต้า 110 สูงกว่าเฟสอัลฟา 211 ส่งผลให้มีเฟสเบต้า 110 มี
 ประสิทธิภาพที่ต่ำ สำหรับการเกิดช่องว่างออกซิเจนบนพื้นผิวตัวเร่งปฏิกิริยา พบว่าประสิทธิภาพ
 ลดลงสำหรับแมงกานีสไดออกไซด์เฟสอัลฟา 211 ในขณะที่การเกิดช่องว่างออกซิเจนในเฟสเบต้า
 110 ช่วยเพิ่มประสิทธิภาพของตัวเร่งปฏิกิริยา สำหรับผลของการเกิดสารมัธยันต์เปอร์ออกไซด์บน
 ตัวเร่งปฏิกิริยาพื้นผิวสมบูรณ์ในปฏิกิริยารีดักชันของออกซิเจน พบว่าเกิดการเสื่อมสภาพบนตัวเร่ง
 ปฏิกิริยาเฟสอัลฟา 211 และเฟสเบต้า 110 นอกจากนี้การเกิดสารมัธยันต์ของเฟสเบต้า 110 มี
 ประสิทธิภาพในปฏิกิริยารีดักชันของออกซิเจนแบบสองอิเล็กตรอนสูงกว่าบนปฏิกิริยารีดักชันของ
 ออกซิเจนแบบสี่อิเล็กตรอน การเกิดสารมัธยันต์ดูดซับบนพื้นผิวตัวเร่งปฏิกิริยานั้นแสดงให้เห็น
 ว่ายังสามารถก่อให้เกิดปฏิกิริยาต่อไปได้ถึงแม้ว่าตัวเร่งปฏิกิริยาจะประกอบไปด้วยการดูดซับของ
 สารมัธยันต์เปอร์ออกไซด์จำนวนมากก็ตาม ดังนั้นการป้องกันไม่ให้เกิดช่องว่างของออกซิเจนบน
 พื้นผิวตัวเร่งปฏิกิริยาแมงกานีสไดออกไซด์อัลฟา 211 เป็นสิ่งสำคัญในการรักษาประสิทธิภาพของ
 ตัวเร่งปฏิกิริยาเฟสอัลฟา 211 ในขณะที่การเกิดช่องว่างของออกซิเจนบนพื้นผิวตัวเร่งปฏิกิริยา
 แมงกานีสไดออกไซด์เบต้า 110 นั้นจะช่วยเพิ่มประสิทธิภาพของตัวเร่งปฏิกิริยาเฟสเบต้า 110

สาขาวิชา วิศวกรรมเคมี
 ปีการศึกษา 2563

ลายมือชื่อนิสิต
 ลายมือชื่อ อ.ที่ปรึกษาหลัก
 ลายมือชื่อ อ.ที่ปรึกษาร่วม
 ลายมือชื่อ อ.ที่ปรึกษาร่วม

6270217821 : MAJOR CHEMICAL ENGINEERING

KEYWORD: Manganese dioxide, Zn-Air battery, oxygen reduction reaction (ORR), density functional theory (DFT)

Puwit Buapin : DEACTIVATION OF MANGANESE DIOXIDE ELECTROCATALYST IN ZINC-AIR BATTERIES STUDIED VIA DENSITY FUNCTIONAL THEORY. Advisor: Asst. Prof. SUPAREAK PRASERTHDAM, Ph.D. Co-advisor: Assoc. Prof. SOORATHEP KHEAWHOM, Ph.D., Meena Rittiruum, Ph.D.

Manganese dioxide (MnO_2) is the effective electrocatalysts used as a cathode for Zn-Air batteries (ZABs) accounted for the acceleration of the oxygen reduction reaction (ORR). There are various studies on the ORR activity of MnO_2 rather than deactivation mechanisms. In this work, the deactivation mechanisms of α - MnO_2 and β - MnO_2 was investigated by density functional theory and computational hydrogen electrode. It was found that, the phase transformation from the α - MnO_2 (211) to β - MnO_2 (110) shows that the catalyst deactivation is due to the higher overpotential of β - MnO_2 (110) making electrocatalyst efficiency low. For O_v surfaces, it illustrates that the performance is decreased in O_v α - MnO_2 (211), while, O_v β - MnO_2 (110) can be enhanced. The poisoning intermediates, $^*\text{OOH}$ found in ORR of perfect catalysts, exhibit deactivation on α - MnO_2 (211) and β - MnO_2 (110). In addition, the activity of poisoning β - MnO_2 (110) on $2e^-$ ORR is higher than that of β - MnO_2 (110) on $4e^-$ ORR. The poisoning intermediate cases reveal that the ORR can operate, although the catalyst surfaces are covered by $^*\text{OOH}$ rich. Therefore, the prevention of O_v for α - MnO_2 is the key to keep the high activity of α - MnO_2 electrocatalysts, while, the O_v can improve the catalytic performance of β - MnO_2 .

Field of Study: Chemical Engineering

Academic Year: 2020

Student's Signature

Advisor's Signature

Co-advisor's Signature

Co-advisor's Signature

ACKNOWLEDGEMENTS

Firstly, I would like to thank the financial fund from Faculty of engineering, Chulalongkorn University and the Center of Excellence on Catalysis and Catalytic Reaction Engineering (CECC), Chulalongkorn University.

I would like to express my special thanks of gratitude to my advisor, Asst. Prof. Supareak Prasertdam, and my co-advisors, Assoc. Prof. Soorathep Kheawhom and Dr. Meena Rittiruam, for their able guidance and support in my thesis.

I express deep and sincere gratitude to my committee members, Prof. Sarawut Rimdusit, Prof. Joongjai Panpranot, Dr. Manaswee Suttipong, and Assoc. Prof. Pornjuk Srepusharawoot.

Finally, my parents and my friends are also an important inspiration for me. So with due regards, I express my gratitude to them.

Puwit Buapin

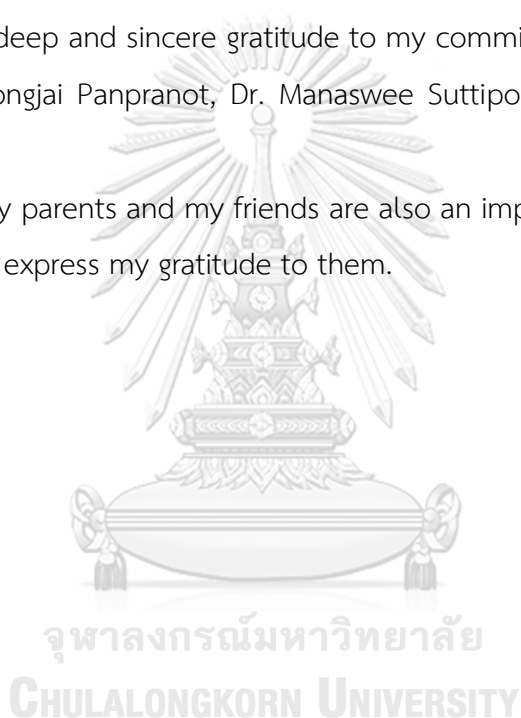


TABLE OF CONTENTS

	Page
.....	iii
ABSTRACT (THAI).....	iii
.....	iv
ABSTRACT (ENGLISH).....	iv
ACKNOWLEDGEMENTS.....	v
TABLE OF CONTENTS.....	vi
LIST OF TABLES.....	viii
LIST OF FIGURES.....	x
Chapter I Introduction.....	1
1.1 Motivation.....	1
1.2 Objective.....	2
1.3 The scope of this research.....	2
Chapter II Background and Literature reviews.....	4
2.1 Zn-Air battery.....	4
2.2 Oxygen reduction reaction.....	4
2.3 Manganese oxide (MnO ₂).....	5
2.4 Density functional theory.....	5
2.5 Literature reviews.....	7
Chapter III Methodology.....	19
3.1 Computational details.....	19
3.1.1 Bulk structures.....	19

3.1.2 Surface models	19
Chapter IV Results and Discussion	24
4.1 Intermediate adsorption on perfect surfaces.....	24
4.2 Intermediate adsorption on oxygen vacancy surfaces.....	29
4.3 Intermediate adsorption on poisoning surfaces	32
4.4 Gibbs free energy diagrams for oxygen reduction reaction.....	33
4.4.1 Spontaneous ORR.....	33
4.4.1.1 Four-electron pathway (pathway I).....	33
4.4.1.2 Two-electron pathway (pathway II).....	36
4.4.2 nonspontaneous ORR (pathway III – VII).....	39
Chapter V Conclusion.....	41
REFERENCES	46
VITA.....	48

LIST OF TABLES

	Page
Table 1 Surface energies for α -MnO ₂ [18].	11
Table 2 Surface energies for β -MnO ₂ [19]	11
Table 3 Oxygen vacancy formation energies of various α -MnO ₂ surface [18].	12
Table 4 Oxygen vacancy formation energies of various β -MnO ₂ surface [19].	12
Table 5 Summary of the ORR Catalytic Performance Revealed from LSV Curves and K-L Plots [8].	13
Table 6 Electron transferred and percent of Hydrogen Peroxide Produced during ORR for Various MnO ₂ Shapes [11].	17
Table 7 Adsorption energy (in eV) of the intermediates: *OOH, *O, *OH, 2*O, *O+*OH, 2*OH for perfect surfaces.	28
Table 8 Bader charge analysis (in e) of the intermediates: *OOH, *O, *OH, 2*O, *O+*OH, 2*OH adsorbing on perfect surfaces.	29
Table 9 Strain (in %) of the intermediates: *OOH, *O, *OH, 2*O, *O+*OH, 2*OH for perfect surfaces.	29
Table 10 Adsorption energy (in eV) of the intermediates: *OOH, *O, *OH for oxygen vacancy surfaces.	31
Table 11 Bader charge analysis (in e) of the intermediates: *OOH, *O, *OH for oxygen vacancy surfaces.	31
Table 12 Strain (in %) of the intermediates: *OOH, *O, *OH for oxygen vacancy surfaces.	31
Table 13 Adsorption energy (in eV) of the intermediates: *OOH, *O, *OH for poisoning surfaces.	33

Table 14 Bader charge analysis (in $|e|$) of the intermediates: *OOH , *O , *OH for vacancy surfaces..... 33

Table 15 Limiting potential (U_L) and overpotential (η) for the four-electron ORR of pathway I on perfect surfaces, oxygen vacancy surfaces, and poisoning surfaces..... 36

Table 16 Limiting potential (U_L) and overpotential (η) for the two-electron ORR of pathway I on perfect surfaces, oxygen vacancy surfaces, and poisoning surfaces..... 39



LIST OF FIGURES

	Page
Figure 1 Deactivation of MnO ₂ triangle.....	3
Figure 2 The ZABs was developed in 2020 [14]	4
Figure 3 Graphical representation of the ORR of ZABs during discharging process [17].	5
Figure 4 Crystal structures of MnO ₂ polymorphs (Mn: magenta and O: red). [17]	5
Figure 5 XRD patterns of different MnO ₂ facets. The symbols: ‘*’ and ‘+’ denote Mn ₃ O ₄ and MnOOH [20].	7
Figure 6 Galvanostatic cycling of the Pt/C+RuO ₂ and MnO ₂ -IL _{0.5} on Zn-air batteries [9].	8
Figure 7 Durability of MnO ₂ and MnO ₂ /CNTs [10].	8
Figure 8 XRD patterns of MnO ₂ at initial and after 1000 cycles [10]. The orange bar is phase of α -MnO ₂ and the pink bar is phase of β -MnO ₂	9
Figure 9 XRD patterns of MnO ₂ /CNTs at initial and after 2000, 4000, 6000, 8000 cycles [10]. The orange bar is phase of α -MnO ₂ and the pink bar is phase of β -MnO ₂	9
Figure 10 Crystal structure of α -MnO ₂ (left) and β -MnO ₂ (right). Red: O and Purple: Mn [18,19].	10
Figure 11 Unit cells containing the slab of β -MnO ₂ [23].	14
Figure 12 Top view of the MnO ₂ (110) surface with lithium adsorbed Mn (purple), O (red) & Li (green) [23].	14
Figure 13 Stable adsorption configurations for two oxygen atoms at the Li/MnO ₂ (110) surface [23].	14

Figure 14 Optimized structures of O ₂ adsorbed on (a) α -MnO ₂ (310), (b) β -MnO ₂ (110), (c) γ -MnO ₂ (120), and (d) δ -MnO ₂ (001). Mn, O(surface), O(adsorbed) are in purple, red, and brown, respectively [34].	15
Figure 15 (a) Free energy diagram for the four-electron associative ORR on Pt (111) and (b) two-electron ORR on PtHg ₄ [21].	16
Figure 16 The XRD patterns of bulk MnO ₂ and the different shapes of MnO ₂ [11].	17
Figure 17 Free energies of different surface slabs of the α -MnO ₂ ·0.25H ₂ O compound in ORR [11].	18
Figure 18 Bulk structure (a) α -MnO ₂ , (b) β -MnO ₂ . Mn and O are indicated blue and red, respectively.	19
Figure 19 Side view of surface models of (a) α -MnO ₂ (110), (b) α -MnO ₂ (200), (c) α -MnO ₂ (211), (d) β -MnO ₂ (101), (e) β -MnO ₂ (110), (f) β -MnO ₂ (211). Mn and O are indicated blue and red, respectively.	20
Figure 20 Top view of surface models (a) α -MnO ₂ (110), (b) α -MnO ₂ (200), (c) α -MnO ₂ (211), (d) β -MnO ₂ (101), (e) β -MnO ₂ (110), (f) β -MnO ₂ (211). The active site for intermediates adsorption during associative ORR highlighted by “*”. Mn and O are indicated blue and red, respectively.	21
Figure 21 Optimized structure of intermediates adsorption for α -MnO ₂ (110). Mn, O, and H indicated in blue, red, and white, respectively.	24
Figure 22 Optimized structure of intermediates adsorption for α -MnO ₂ (200). Mn, O, and H indicated in blue, red, and white, respectively.	25
Figure 23 Optimized structure of intermediates adsorption for α -MnO ₂ (211). Mn, O, and H indicated in blue, red, and white, respectively.	25
Figure 24 Optimized structure of intermediates adsorption for β -MnO ₂ (101). Mn, O, and H indicated in blue, red, and white, respectively.	26
Figure 25 Optimized structure of intermediates adsorption for β -MnO ₂ (110). Mn, O, and H indicated in blue, red, and white, respectively.	26

Figure 26 Optimized structure of intermediates adsorption for β -MnO ₂ (211). Mn, O, and H indicated in blue, red, and white, respectively.....	27
Figure 27 Top surface in terms of electron accumulation (yellow region) and electron depletion regions of (a) O _v - α -MnO ₂ (211) and (b) O _v - β -MnO ₂ (110), as isovalue ± 0.012 e/Å ³ . O _v positions were highlighted by *. Mn and O are indicated by blue and red, respectively.	30
Figure 28 Optimized structure of intermediates adsorption (*OOH, *O, and *OH) for (a-c) O _v - α -MnO ₂ (211) and (d-f) O _v - β -MnO ₂ (110). Mn, O, and H indicated in blue, red, and white, respectively.	31
Figure 29 Optimized structure of intermediates adsorption (*OOH, *O, and *OH) for (a-c) poisoning- α -MnO ₂ (211) and (d-f) poisoning- β -MnO ₂ (110). Mn, O, and H indicated in blue, red, and white, respectively.....	32
Figure 30 Relative free energy diagram for the four-electron associative ORR mechanism of pathway I on various perfect surfaces including of (a) α -MnO ₂ (100), (b) α -MnO ₂ (200), (c) α -MnO ₂ (211), (d) β -MnO ₂ (101), (e) β -MnO ₂ (110), and (f) β -MnO ₂ (211).....	34
Figure 31 Relative free energy diagram for the four-electron associative ORR of pathway I on (a) O _v - α -MnO ₂ (211), (b) O _v - β -MnO ₂ (110), (c) poisoning- α -MnO ₂ (211), and (d) poisoning- β -MnO ₂ (110).	35
Figure 32 Ternary plots of the overpotential on 4e ⁻ ORR pathway for (a) α -MnO ₂ (211) (b) β -MnO ₂ (101).....	36

Chapter I Introduction

1.1 Motivation

Nowadays, the increase of energy consumption represents the largest sources of greenhouse gas emission from human activities, such as using oil for the car, coal-burning for generate electricity, and so on. Renewable energy is one of the solutions for staving off the effect of global warming because it is collected from renewable resources including hydropower, wind energy, and solar energy [1]. Renewable energy sources such as water and solar not emit greenhouse gases [2]. Moreover, it could help decreasing the electricity emissions by about 81 percent [3]. Batteries play important roles in daily life, stored from the initial energy as a backup electrical energy source such as telecommunication and transportation. Rechargeable batteries have a power from the renewable resource because they allow the energy released in discharging process while stored in charging process. Despite recently commercial batteries, lithium-ion batteries (LIBs) are still suffered from low efficient energy density (350 W h kg^{-1}) [4]. Moreover, the stability of LIBs was not too high in a long time of using [5]. So, researchers have studied improving the performance of batteries. As a possible alternative, zinc-air batteries (ZABs) have become of increased interest recently due to their large theoretical energy density (1353 W h kg^{-1}), low-cost, and safety [4]. The electrochemical reaction involving charging and discharging in a cathode of ZABs is oxygen evolution reaction (OER) and oxygen reduction reaction (ORR). For the OER, this reaction is very fast, while the ORR is crucial in view of its practical applications in the output energy. The ORR has two possible pathways: (1) the four-electron ($4e^-$) pathway, where oxygen was reduced to H_2O in acidity or OH^- in medium and (2) the two-electron ($2e^-$) pathway involving partial reduction of oxygen to form hydrogen peroxide (H_2O_2). So, the ORR plays crucial role for the performance on ZABs because the number of electron transfer affects to the power output in ZABs. At the beginning, Pt-based material is one of the most catalysts that are used for commercial electrocatalyst. Yet, the limited performance and the high cost of Pt led to explore the new catalysts. Manganese oxide (MnO_2) is an excellent interesting catalyst because it is abundant, inexpensive, nontoxic [6], and high activity on ORR [30]. Matsuki *et al.* [7] found the

rate of ORR on MnO_2/C through the current is higher than Pt catalyst. Meng et al. reported the number of electron transfer on ORR is 4.2 on $\alpha\text{-MnO}_2$ and 2.4 on $\beta\text{-MnO}_2$ [8]. For deactivation of a catalyst, Gu et al. [9] studied the long term of cycling performance on MnO_2 using ionic liquid compared with Pt, the result showed that the stability of MnO_2 is higher than Pt. Xu et al. [10] studied the cycle of ZAB during 1000 cycles, and the XRD result showed that the initial phase, $\alpha\text{-MnO}_2$, altered to $\beta\text{-MnO}_2$ after the operation. Also, $\alpha\text{-MnO}_2$ (110) and $\alpha\text{-MnO}_2$ (200) disappeared during the long operation. From the XRD analysis [11,12], the (211) facet is the main surface of $\alpha\text{-MnO}_2$, while the (101) facet is found as the main surface of $\beta\text{-MnO}_2$. Due to the ORR that has many intermediate species: $^*\text{OOH}$, $^*\text{O}$, $^*\text{OH}$. It is difficult to detect them by an experiment. Moreover, deactivation of MnO_2 electrocatalyst still exist. Herein, density functional theory (DFT) calculation and the computer hydrogen electrode (CHE) have been employed to investigate the deactivation of MnO_2 electrocatalyst on ORR both $4e^-$ and $2e^-$ pathways and its performance for ZABs. The activity and stability of various MnO_2 are demonstrated in term of phase transformation, oxygen vacancy, and poisoning intermediates.

1.2 Objective

This work aimed to study deactivation of MnO_2 catalyst used as a cathode in Zn-Air batteries by density functional theory calculation.

1.3 The scope of this research

1.3.1 The surface models used in this work are $\alpha\text{-MnO}_2$ (110), $\alpha\text{-MnO}_2$ (200), $\alpha\text{-MnO}_2$ (211), $\beta\text{-MnO}_2$ (101), $\beta\text{-MnO}_2$ (110), and $\beta\text{-MnO}_2$ (211).

1.3.2 The reaction is studied on the $4e^-$ and $2e^-$ pathways of oxygen reduction reaction.

1.3.3 The computational hydrogen electrode (CHE) is employed to investigate the free energy of the ORR.

1.3.4 The deactivation studied is phase transformation, oxygen vacancy, and poisoning intermediates.

Figure 1. shows the deactivation relation among phase transformation, oxygen vacancy defect, and poisoning intermediates.

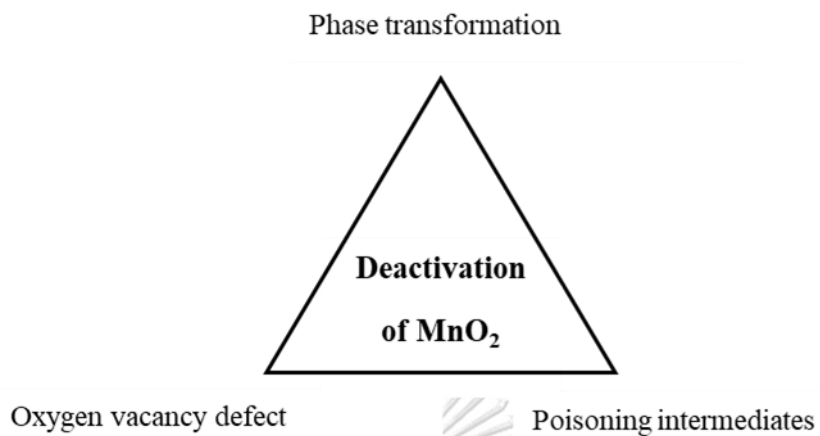


Figure 1 Deactivation of MnO₂ triangle



Chapter II Background and Literature reviews

2.1 Zn-Air battery

Zn-air batteries (ZABs) are an interesting energy storage system. The concept was reported by Smee in 1840. In 1878, Maiche presented primary ZABs using a porous carbon as a cathode. The primary ZABs were introduced for commercial products in 1932. It has high energy density ($200\text{--}500\text{ W h kg}^{-1}$) but still low output power performance [5]. Rechargeable ZABs consist of Zn as an anode, a separator, and air through pass the cathode side, packaged with the aqueous alkaline electrolyte such as KOH. The generation of electricity in rechargeable ZABs is realized on the ORR and OER [13]. The ZABs being deployed in New York as shown Figure 2 for very low cost, \$45/kWh [14].



Figure 2 The ZABs developed in 2020 [14]

2.2 Oxygen reduction reaction

The ORR is one of the most important electrochemical reactions affecting in energy storage systems in ZABs. The ORR reaction on both sides of cathode is shown in Figure 3. The ORR has two possible pathways: the ORR $4e^-$ pathway, where oxygen is converted to OH^- by complete reduction and the $2e^-$ pathway showing O_2 was reduced to generate hydrogen peroxide (H_2O_2) [15]. The ORR has many intermediates, $^*\text{O}$, $^*\text{OOH}$, $^*\text{OH}$. The ORR mechanism in MnO_2 catalyst has been widely studied. It was proposed that ORR $2e^-$ pathway on MnO_2 catalyst at low cathodic overpotential, and ORR $4e^-$ pathway at high overpotential [16].

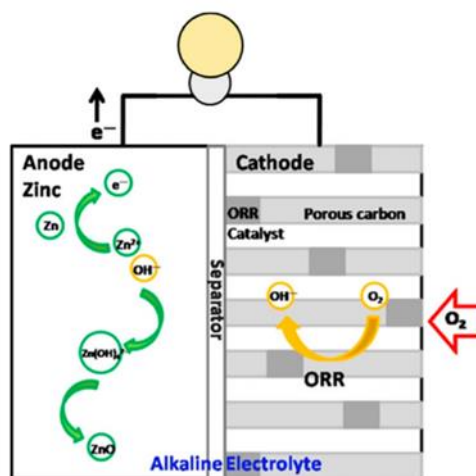


Figure 3 Graphical representation of the ORR of ZABs during discharging process [17].

2.3 Manganese oxide (MnO_2)

MnO_2 is a material that used in the electrical energy storage system because manganese is cheap and abundant in the earth's crust. There are six polymorphs of manganese oxide: α - MnO_2 , β - MnO_2 , R - MnO_2 , γ - MnO_2 , δ - MnO_2 , and λ - MnO_2 as illustrated in Figure 4. [17]

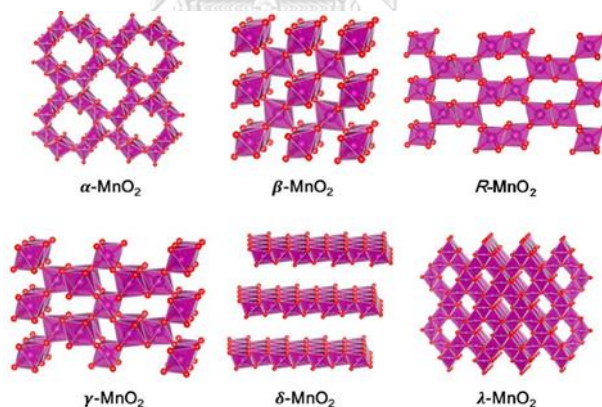


Figure 4 Crystal structures of MnO_2 polymorphs (Mn: magenta and O: red). [17]

2.4 Density functional theory

Density functional theory, DFT, is a method for examining molecules, nanostructures, solids, surfaces, and interfaces through the directly unraveling approximate of the Schrödinger equation. The DFT starts from the many-body Schrödinger equation to Hartree-Fock equation, Kohn-Sham equation as well as self-

consistent calculation. The time-independent Schrödinger equation yields the following symbolic form:

$$(\text{kinetic energy} + \text{potential energy})\Psi = E_{\text{tot}}\Psi \quad (1)$$

where E_{tot} is the total energy for the wavefunction Ψ

The potential function for one electron $V(\mathbf{r})$ can be written as:

$$\left(\frac{p^2}{2m_e} + V(\mathbf{r})\right)\Psi(\mathbf{r}) = E_{\text{tot}}\Psi(\mathbf{r}) \quad (2)$$

where m_e , \mathbf{p} is an electron mass are the quantum-mechanical momentum operator. The probability of finding the particle at the point \mathbf{r} is $|\Psi(\mathbf{r})|$

The quantum-mechanical momentum operator (\mathbf{p}) is given by:

$$\mathbf{p} = -i\hbar\nabla \quad (3)$$

$$\nabla = \mathbf{u}_x \frac{\partial}{\partial x} + \mathbf{u}_y \frac{\partial}{\partial y} + \mathbf{u}_z \frac{\partial}{\partial z} \quad (4)$$

where \hbar is Dirac constant.

The lowest energy solution of an equation is defined as Ψ_0 and the electron charge distribution at equilibrium is given by $|\Psi_0(\mathbf{r})|$. The integral of the electronic charge density during the material yields the number of electrons, N defined as:

$$N = \int \rho(\mathbf{r})d\mathbf{r} \quad (5)$$

where $\rho(\mathbf{r})$ is the electron density which simple evaluate by the charge density $n(\mathbf{r})$ defined as:

$$\rho(\mathbf{r}) = \sum \int |\Psi_0(\mathbf{r})|^2 d\mathbf{r} \quad (6)$$

The kinetic energy for N electrons and M nuclei can be written as:

$$\text{kinetic energy} = -\sum_{i=1}^N \frac{\hbar^2}{2m_e} \nabla_i^2 - \sum_{I=1}^M \frac{\hbar^2}{2M_I} \nabla_I^2 \quad (7)$$

where $M_I = M_1, M_2, M_3, \dots$ is a mass of nuclei.

The potential energy term can be express in eq. (8-10)

$$(\text{potential energy})_{ee} = \frac{1}{2} \sum_{i \neq j}^N \frac{e^2}{4\pi\epsilon_0} \frac{1}{|r_i - r_j|} \quad (8)$$

$$(\text{potential energy})_{nn} = \frac{1}{2} \sum_{I \neq J}^M \frac{e^2}{4\pi\epsilon_0} \frac{Z_I Z_J}{|R_I - R_J|} \quad (9)$$

$$(\text{potential energy})_{en} = \sum_{i,I}^N \frac{e^2}{4\pi\epsilon_0} \frac{Z_I}{|r_i - R_I|} \quad (10)$$

The many-body Schrödinger equation is written as:

$$\left(-\sum_{i=1}^N \frac{\hbar^2}{2m_e} \nabla_i^2 - \sum_{i=1}^M \frac{\hbar^2}{2M_i} \nabla_i^2 + \frac{1}{2} \sum_{i \neq j}^N \frac{e^2}{4\pi\epsilon_0} \frac{1}{|r_i - r_j|} + \frac{1}{2} \sum_{I \neq J}^N \frac{e^2}{4\pi\epsilon_0} \frac{Z_I Z_J}{|R_I - R_J|} + \sum_{i,I}^N \frac{e^2}{4\pi\epsilon_0} \frac{Z_I}{|r_i - R_I|} \right) \Psi(\mathbf{r}) = E_{\text{tot}} \Psi(\mathbf{r}) \quad (11)$$

The nuclear coordinates disappear completely as following:

$$\left[-\sum_i \frac{\nabla_i^2}{2} + \sum_i V_n(\mathbf{r}) + \frac{1}{2} \sum_{i \neq j} \frac{1}{|r_i - r_j|} \right] \Psi = E \Psi \quad (12)$$

The simple Kohn-Sham equation for single particle can be written as:

$$\left[-\frac{\nabla^2}{2} + V_n(\mathbf{r}) + V_H(\mathbf{r}) + V_x(\mathbf{r}) + V_c(\mathbf{r}) \right] \phi_i(\mathbf{r}) = \epsilon_i \phi_i(\mathbf{r}) \quad (13)$$

where V_H , V_x , and V_c are Hartree-Fock potential, exchange potential, and correlation potential, respectively.

The energy of this state E is calculated by:

$$E = \int d\mathbf{r}_1, d\mathbf{r}_2, \dots, d\mathbf{r}_N \Psi^*(\mathbf{r}_1, \mathbf{r}_2, \dots, \mathbf{r}_N) H \Psi(\mathbf{r}_1, \mathbf{r}_2, \dots, \mathbf{r}_N) \quad (14)$$

The DFT concept is an observation when E is the lowest possible energy of the system.

2.5 Literature reviews

Cheng *et al.* [20] studied oxygen reduction reaction on MnO_2 with oxygen vacancies. They found that (101), (110), and (211) are the majority facets of β - MnO_2 from XRD patterns as shown in Figure 5. Moreover, the MnO_2 with oxygen vacancies capacitates more positive potential, larger current, and lower peroxide yield for the ORR.

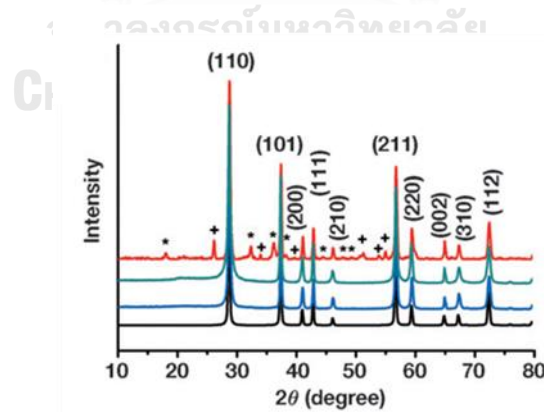


Figure 5 XRD patterns of different MnO_2 facets. The symbols: '*' and '+' denote Mn_3O_4 and MnOOH [20].

Gu *et al.* [9] studied the efficient catalysts for ORR and OER on α - MnO_2 synthesized using ionic liquid (IL) as the structure-directing agent and β - MnO_2 . While increasing the concentration of IL, the transformation products is from β - MnO_2 to α -

MnO₂. For both ORR and OER, the activity of α -MnO₂ is higher than that of β -MnO₂. Moreover, the comparison of stability between MnO₂ and Pt catalyst is shown in Figure 6. The voltage on MnO₂-IL_{0.5} exhibits more stable during the long operation, while the Pt/C+RuO₂ is stable only 15 hr.

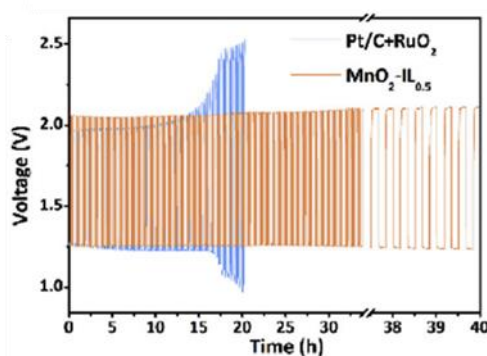


Figure 6 Galvanostatic cycling of the Pt/C+RuO₂ and MnO₂-IL_{0.5} on Zn-air batteries [9].

Xu *et al.* [10] studied the carbon nanotubes (CNTs) doped MnO₂ catalyst. The ORR and OER performance on MnO₂/CNTs catalyst shows excellent stability that are identical after 2000 cycles as shown in Figure 7, while the current density of MnO₂ changed during 1000 cycles. From the XRD result in Figure 8, the major crystal structure of initial MnO₂ is the α -MnO₂(211). After 1000 cycles of operation, the β -MnO₂(110) is the main surface. So, the phase transformation is from α -MnO₂ to β -MnO₂. The XRD result of MnO₂/CNTs is shown in Figure 9 The initial phase of MnO₂/CNTs and phase after long operation (2000, 4000, 6000, and 8000 cycles) is not different. In addition, no phase transformation effect for MnO₂/CNTs.

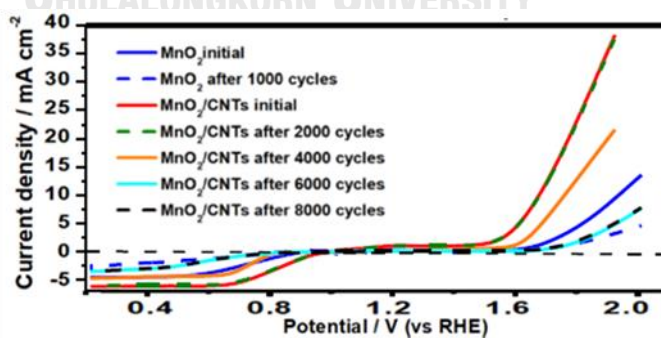


Figure 7 Durability of MnO₂ and MnO₂/CNTs [10].

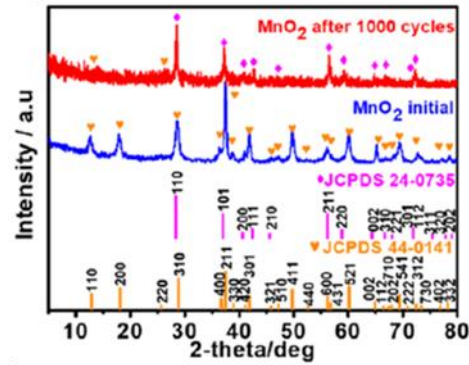


Figure 8 XRD patterns of MnO_2 at initial and after 1000 cycles [10]. The orange bar is phase of $\alpha\text{-MnO}_2$ and the pink bar is phase of $\beta\text{-MnO}_2$.

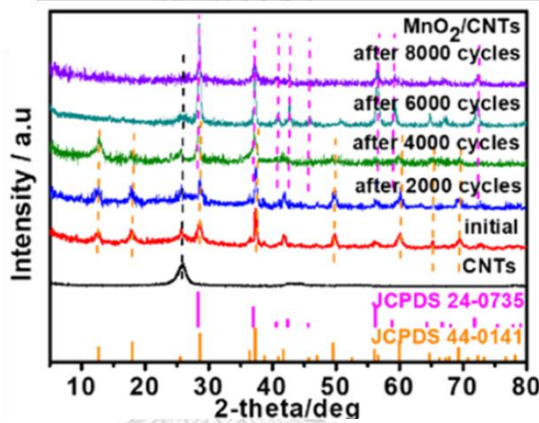


Figure 9 XRD patterns of MnO_2/CNTs at initial and after 2000, 4000, 6000, 8000 cycles [10]. The orange bar is phase of $\alpha\text{-MnO}_2$ and the pink bar is phase of $\beta\text{-MnO}_2$.

David *et al.* [18,19] studied surfaces properties of $\alpha\text{-MnO}_2$ and $\beta\text{-MnO}_2$. $\alpha\text{-MnO}_2$ and $\beta\text{-MnO}_2$ have been demonstrated to produce high capacitance as supercapacitor in ZABs. The bulk structures of $\alpha\text{-MnO}_2$ and $\beta\text{-MnO}_2$ as shown in Figure 10. The catalytic and surfaces properties of materials are essential that the characteristics of the experimental data. After optimization, Lattice parameters of $\alpha\text{-MnO}_2$ are $a = 4.442 \text{ \AA}$, $b = 4.442 \text{ \AA}$, and $c = 2.933 \text{ \AA}$. For $\beta\text{-MnO}_2$, lattice parameters are $a = 9.907 \text{ \AA}$, $b = 9.907 \text{ \AA}$, and $c = 2.927 \text{ \AA}$. Surface energies can be calculated in eq. (15)

$$\gamma = \frac{E_s - nE_b}{2A} \quad (15)$$

where E_s and E_b are the energy of a slab containing n formula units and the total energy per formula unit of bulk $\alpha\text{-MnO}_2$, respectively. A is the area of the slab surface. Surface energies for $\alpha\text{-MnO}_2$ are shown in Table 1, in which the (100) and (110)

of α -MnO₂ show low surface energies, 0.64 and 0.75 J m⁻², respectively. The calculated surface energy for the (310) surface is 1.41 J m⁻², high surface energy, it is likely to be unstable surface. Surface energies for β -MnO₂ are shown in Table 2. The (110) of β -MnO₂ exhibits the most stable surface with its surface energy of 0.62 J m⁻². The oxygen vacancy formation energies of various α -MnO₂ and β -MnO₂ surfaces are shown in Table 3 and Table 4, respectively. α -MnO₂ has catalytic activity higher than that of β -MnO₂. The oxygen vacancy of β -MnO₂ is more stable than that of α -MnO₂. In addition, the calculated oxygen vacancy formation energies on various surfaces by approximately 1 eV are lower than that of various β -MnO₂ surfaces.

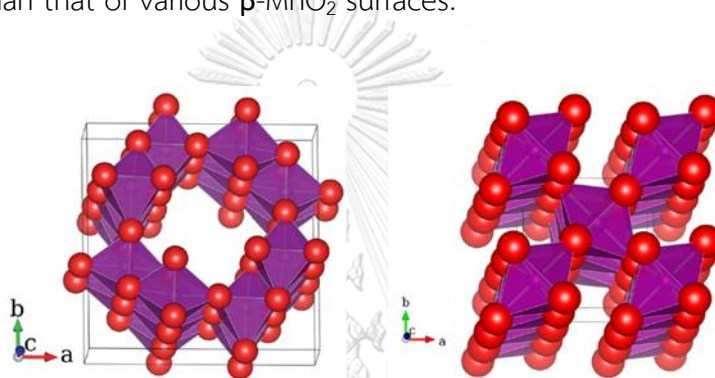


Figure 10 Crystal structure of α -MnO₂ (left) and β -MnO₂ (right). Red: O and Purple: Mn [18,19].

Table 1 Surface energies for α -MnO₂ [18].

Miller index	surface energy (J m ⁻²)
(100)	0.64
(001)	1.76
(110)	0.75
(111)	1.32
(101)	1.91
(102)	1.55
(112)	1.40
(122)	1.54
(201)	1.51
(211)	1.08
(221)	1.59
(310)	1.41

Table 2 Surface energies for β -MnO₂ [19]

Miller index	surface energy (J m ⁻²)
(100)	0.94
(001)	1.80
(110)	0.62
(111)	1.42
(101)	1.59
(201)	1.41
(211)	1.12
(221)	2.54
(311)	1.08
(321)	1.01
(331)	3.59

Table 3 Oxygen vacancy formation energies of various α -MnO₂ surface [18].

Miller index	ΔE_f (O-vac) (eV)
(100)	1.02
(110)	0.97
(111)	0.30
(211)	1.09
(112)	0.07
Bulk	2.57

Table 4 Oxygen vacancy formation energies of various β -MnO₂ surface [19].

Miller index	ΔE_f (O-vac) (eV)
(100)	1.02
(110)	0.97
(111)	0.30
(211)	1.09
(112)	0.07
Bulk	2.57

Li *et al.* [16] investigated the effect of oxygen vacancies on the surface and catalytic activity of β -MnO₂ for ORR through a combination of experiments and DFT+U calculation. The important DFT parameters are that (1) the U value is 4 eV, (2) the cutoff energy of 380 eV was selected in this work, and (3) a 3×3×3 Monkhorst–Pack k-point mesh was used for the Brillouin zone integration. After optimized the vacancy surface of β -MnO₂, they found that the oxygen vacancies have a little impact on the proton insertion process of defective MnO₂.

Yongtao *et al.* [8] studied the number of electrons transferred per oxygen molecule, which was calculated as shown in Table 5. The number of electrons transferred are 4.2, 3.7, and 3.9 for α -MnO₂-SF, α -MnO₂-HT, and Ni/ α -MnO₂-SF, respectively, where SF and HT defined as solvent free method and hydrothermal method, respectively. So, α -MnO₂ adopts an 4e⁻ ORR pathway. Moreover, the number

of electrons transferred are 2.5, 2.4, and 1.7 for AMO, β -MnO₂, and δ -MnO₂, respectively, which suggests an $2e^-$ ORR transfer instead.

Table 5 Summary of the ORR Catalytic Performance Revealed from LSV Curves and K-L Plots [8].

Catalyst	The number of electrons transfer
α -MnO ₂ -SF	4.2
α -MnO ₂ -HT	3.7
Ni/ α -MnO ₂ -SF	3.9
AMO	2.5
β -MnO ₂	2.4
δ -MnO ₂	1.7

Xilin *et al.* [22] studied the overpotential towards ORR and OER on the metal doped graphene-based catalysts. They found that the activity on Co site of CoN_x-gra (x=1, 2, 3, and 4) would be affected by both the N-dopant concentration and configuration. The free energy of O₂ was set to 4.92 eV by the reaction: 2H₂O → O₂ + 2H₂. The overpotential can be calculated by eq. (16). The CoN₄-gra is identified as the best candidate with the calculated overpotential of 0.47 eV for the ORR and 0.69 eV for OER. While the worst catalyst of this work is CoN₂-O, the maximum overpotential of ORR, 1.10 eV.

$$\eta = \frac{\max(\Delta G_a, \Delta G_b, \Delta G_c, \Delta G_d)}{e} - 1.23 \quad (16)$$

Thomas *et al.* [23] studied the surface models of β -MnO₂ as shown in Figure. 11. The most stable various plane of β -MnO₂ is (110) facet, surface energy of β -MnO₂ (110) is 1.151 J m⁻². Moreover, the adsorption of Li atom on β -MnO₂ (110) was studied as shown in Figure. 12. Adsorption energies of three positions with Li adsorbed at bbi, bbi(nnn), and bii(nn) site are -1.80 eV, -1.76 eV, and -1.62 eV, respectively. The four different stable models of two oxygen atoms adsorption on the Li/MnO₂ (110) were studied, which are shown in Figure. 13. Adsorption energies of dissociated, peroxo on Mn, peroxo on Li, and peroxo on Mn/Li are -2.25 eV, -2.00 eV, -1.81 eV, and -1.27 eV, respectively.

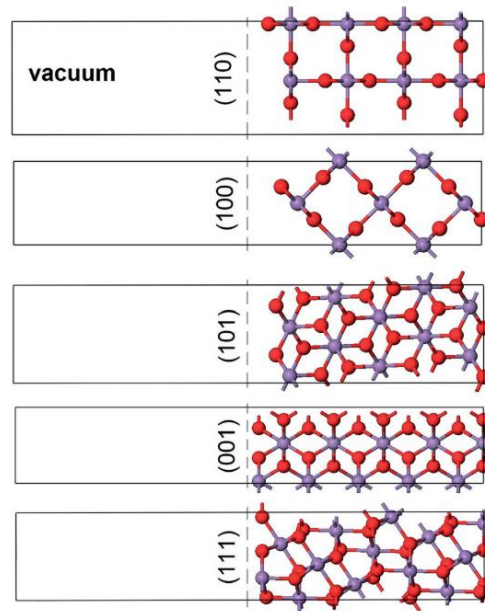


Figure 11 Unit cells containing the slab of β - MnO_2 [23].

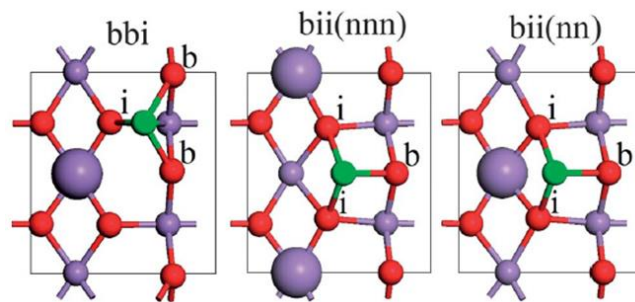


Figure 12 Top view of the MnO_2 (110) surface with lithium adsorbed Mn (purple), O (red) & Li (green) [23].

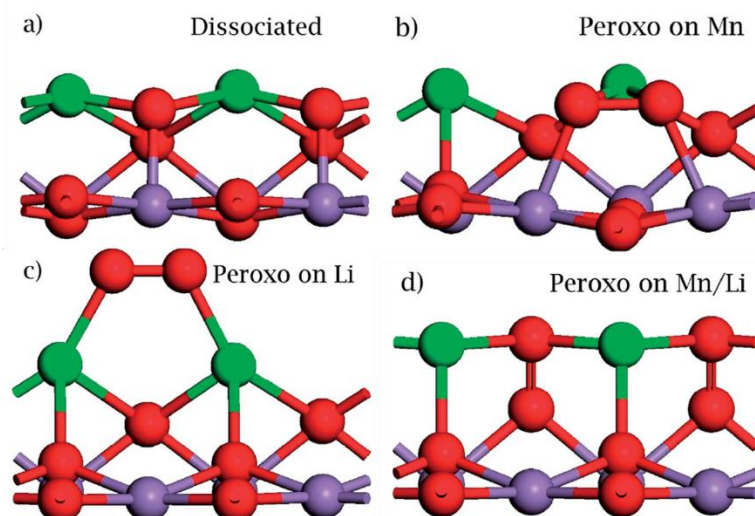


Figure 13 Stable adsorption configurations for two oxygen atoms at the Li/MnO_2 (110) surface [23].

Yujie *et al.* [34] studied the catalytic performance of crystal plane MnO_2 for the total oxidation of propane via DFT. The adsorption of oxygen at the O vacancy on MnO_2 catalyst is shown in Figure. 14. The adsorption energy of O_2 on α - MnO_2 (310), β - MnO_2 (110), γ - MnO_2 (120), and δ - MnO_2 (001) are 1.02, 0.88, 1.17, and 1.55 eV, respectively. The O-O bond distance of adsorbed O_2 on α - MnO_2 (310), β - MnO_2 (110), γ - MnO_2 (120), and δ - MnO_2 (001) are 1.313, 1.305, 1.310, and 1.317 Å, respectively, where those increased from 1.21 Å (isolated oxygen molecule). These provide the evidence that O_2 is activated to O_2^- and oxygen can be activated on the defect surfaces of various MnO_2 .

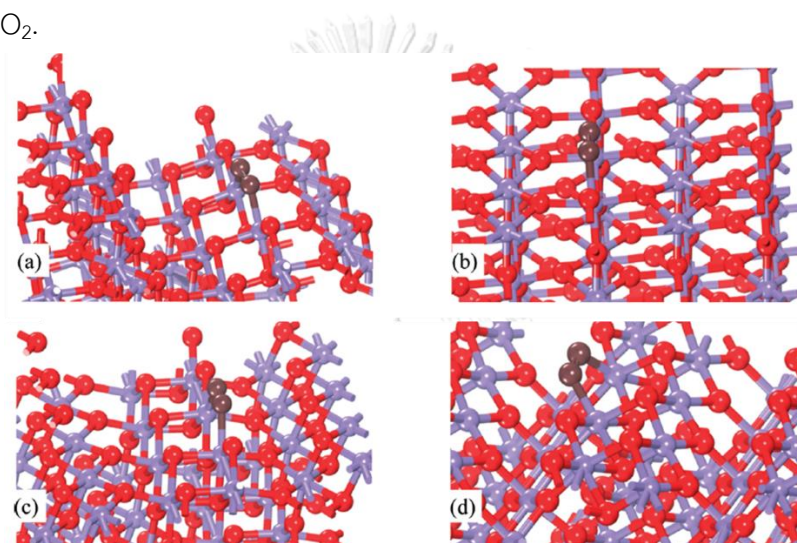


Figure 14 Optimized structures of O_2 adsorbed on (a) α - MnO_2 (310), (b) β - MnO_2 (110), (c) γ - MnO_2 (120), and (d) δ - MnO_2 (001). Mn, O(surface), O(adsorbed) are in purple, red, and brown, respectively [34].

Ambarish *et al.* [21] showed free energy diagram for the $4e^-$ ORR pathway on Pt (111) and $2e^-$ ORR pathway on PtHg_4 in Figure. 15. For $4e^-$ ORR pathway, at equilibrium potential $U=1.23$ V (green line), the step from O_2 to $^*\text{OOH}$ is nonspontaneous so the maximum potential that made all chemical reactions spontaneous is $U=0.75$ V, the limiting potential. For $2e^-$ ORR pathway, the limiting potential is $U=0.64$ V.

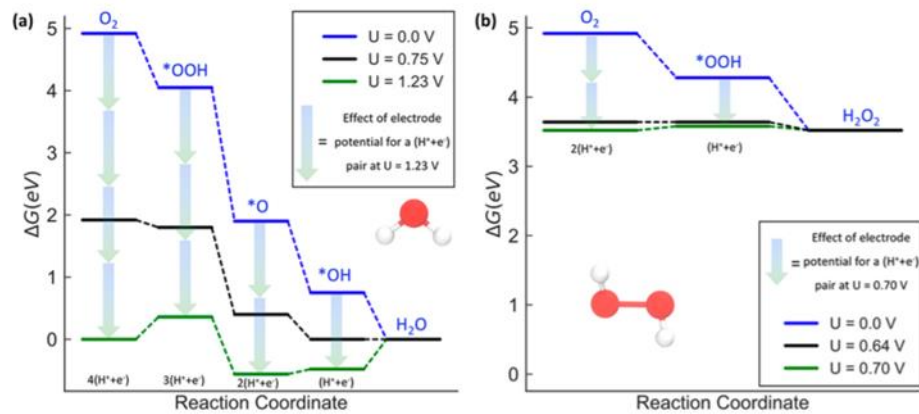
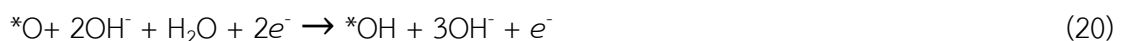
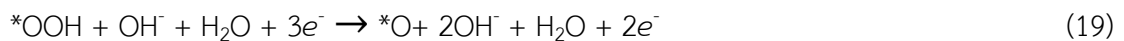
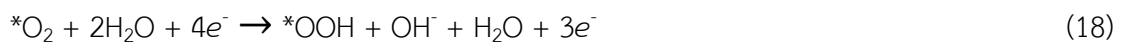
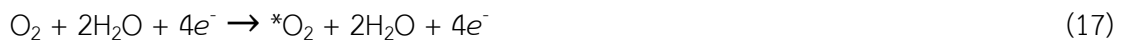


Figure 15 (a) Free energy diagram for the four-electron associative ORR on Pt (111) and (b) two-electron ORR on PtHg₄ [21].

Karupppiah *et al.* [11] studied the number of electrons transferred during oxygen reduction reaction. The XRD patterns of bulk α -MnO₂ and different shapes of MnO₂ is shown in Figure 16. The nano flowers contain the (110) facet, the major facet, while the (211) facet found in nanowires shape. The electron transfers in ORR are calculated from K-L plots at -0.8 V, the result as shown in Table 6. The electron transfer is 3.5 that is very close to a 4e⁻ ORR pathway. In contrast, the electrons transferred result for MnO₂ nanoflower catalyst is 1.9 and 2.3 for α -MnO₂ nanoparticle. In both cases, the electron transfer is close to 2.0, which refers to a 2e⁻ ORR pathway for flower and particle shapes. In addition, the nanowire is the best shape because the number of electron transfer is closed to 4 and the percent of H₂O₂ is very low. Moreover, the relative free energy for different surfaces of α -MnO₂ is shown if Figure. 17. The elementary steps of ORR represent in eq. (17-21)



The pH value for calculating Gibbs free energy is pH = 13 as the 0.1 M KOH electrolyte in this work. From the result, it implies that the adsorption of O₂ and reduction toward OOH⁻ are nonspontaneous and other elementary steps are spontaneous, so the rate-limiting step is the reduction of OOH⁻.

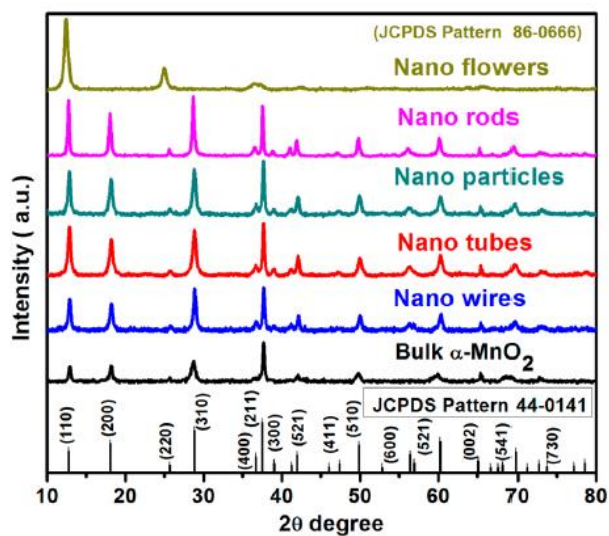


Figure 16 The XRD patterns of bulk MnO_2 and the different shapes of MnO_2 [11].

Table 6 Electron transferred and percent of Hydrogen Peroxide Produced during ORR for Various MnO_2 Shapes [11].

Sample	The number of electrons transfer at -0.8 V (SCE)	% H_2O_2 produced at -0.8 V (SCE)
Nanowires	3.5	3.66
Nanotubes	3.0	21.44
Nanoparticles	2.3	39.50
Nanorods	3.2	1.97
nanoflowers	1.9	23.89
Bulk- MnO_2	1.6	106.38

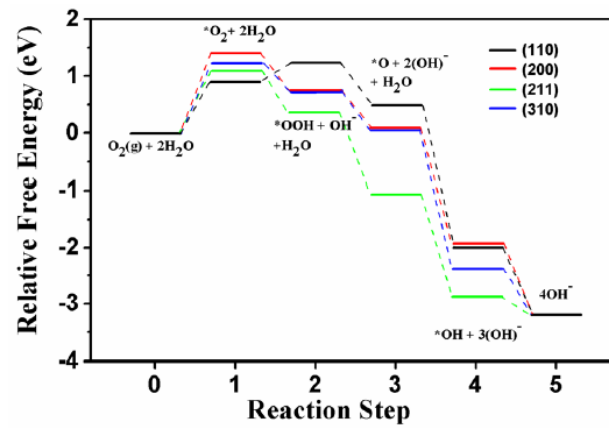


Figure 17 Free energies of different surface slabs of the $\alpha\text{-MnO}_2\cdot 0.25\text{H}_2\text{O}$ compound in ORR [11].



Chapter III Methodology

3.1 Computational details

The total energy calculation was performed under the DFT-based implemented in the Vienna Ab initio Simulation Package (VASP) [24-27]. The exchange-correlation function based on the projector augmented wave (PAW) and the Perdew–Burke–Erzerhoff generalized gradient (PBE-GGA) [28] was used. The energy cutoff is 500 eV. The DFT+U calculation was performed using $U = 1.6$ eV for Mn [29,30]. The Van der Waals dispersion-corrected DFT (DFT–D3) [31] was used for all calculations. All calculations performed the structural optimization method under 0.05 eV/Å of force convergence.

3.1.1 Bulk structures

The bulk structures of α -MnO₂ and β -MnO₂ is illustrated in Figure 18. These were designed using the crystal structure data of space group number 87 for α -MnO₂ [32] and 136 for β -MnO₂ [33]. The k-point value used for bulk calculation is $5 \times 5 \times 5$. The calculated lattice parameters are $a=9.8252$ Å, $b=9.8252$ Å, and $c=2.8868$ Å for α -MnO₂, $a=4.4358$ Å, $b=4.4358$ Å, and $c=2.9024$ Å for β -MnO₂.

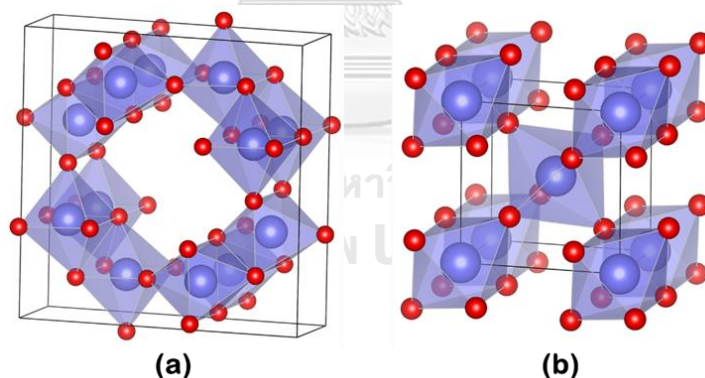


Figure 18 Bulk structure (a) α -MnO₂, (b) β -MnO₂. Mn and O are indicated blue and red, respectively.

3.1.2 Surface models

The surface models of α -MnO₂ (110), α -MnO₂ (200), α -MnO₂ (211), β -MnO₂ (101), β -MnO₂ (110), and β -MnO₂ (211) are illustrated in Figure 19. In the Monkhorst-Pack k-mesh Brillouin-zone integration, the $3 \times 3 \times 1$ was used for all surface models during the optimization. The cell dimensions ($a \times b \times c$) are as followed: $3 \times 2 \times 1$ for α -MnO₂ (110), $3 \times 2 \times 1$ for α -MnO₂ (200), $1 \times 1 \times 1$ for α -MnO₂ (211), $2 \times 2 \times 1$ for β -MnO₂ (101), $2 \times 3 \times 1$ for

β -MnO₂ (110), and 3×3×1 for β -MnO₂ (211) surfaces, respectively. All surface models have vacuum space approximately 20 Å along c-axis.

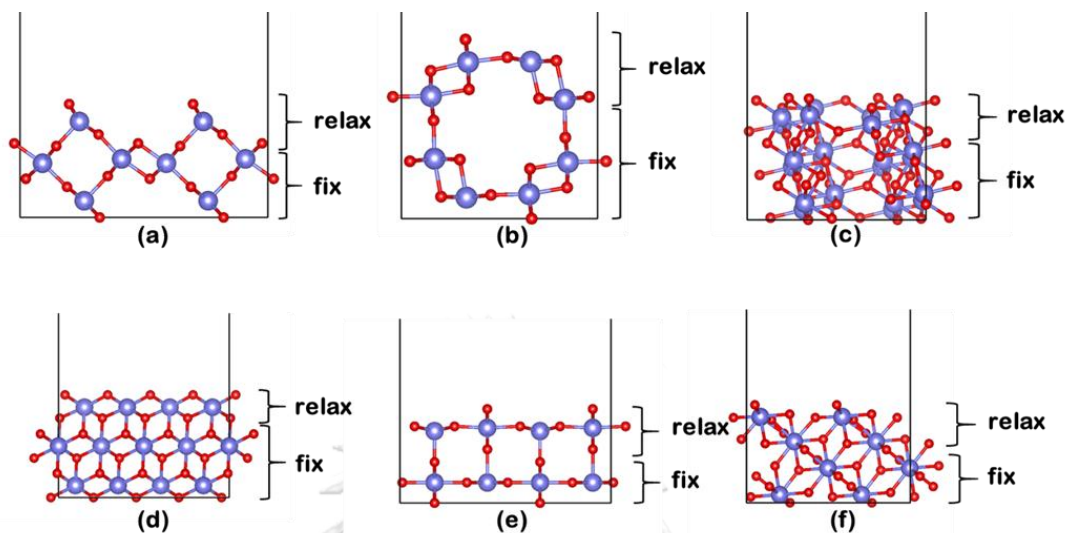


Figure 19 Side view of surface models of (a) α -MnO₂(110), (b) α -MnO₂(200), (c) α -MnO₂(211), (d) β -MnO₂(101), (e) β -MnO₂(110), (f) β -MnO₂(211). Mn and O are indicated blue and red, respectively.

The top view of surface models of α -MnO₂ (110), α -MnO₂ (200), α -MnO₂ (211), β -MnO₂ (101), β -MnO₂ (110), and β -MnO₂ (211) is shown in Figure 20.

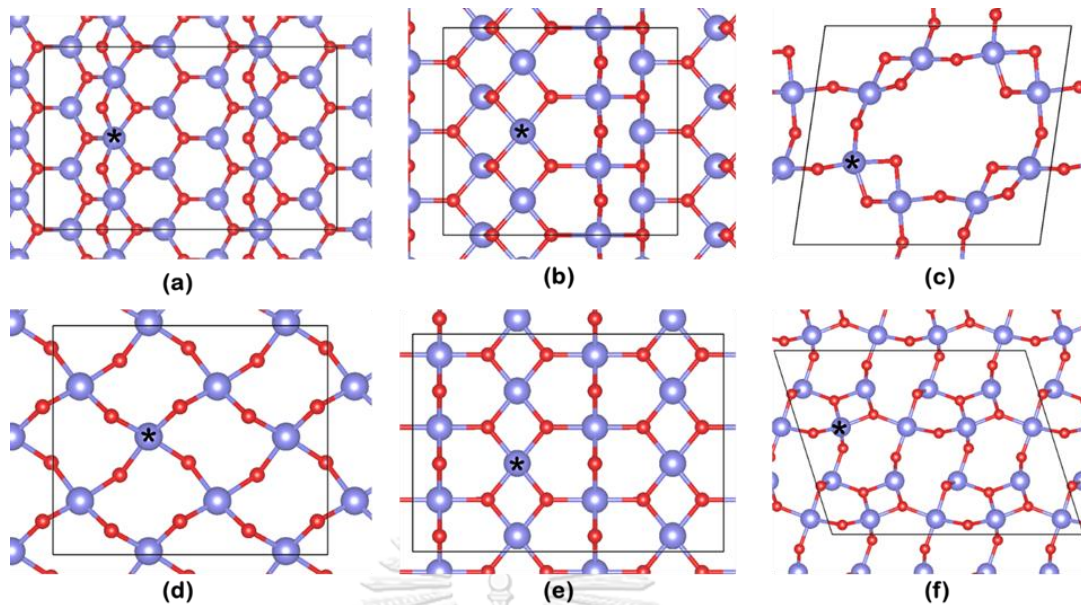


Figure 20 Top view of surface models (a) α - $\text{MnO}_2(110)$, (b) α - $\text{MnO}_2(200)$, (c) α - $\text{MnO}_2(211)$, (d) β - $\text{MnO}_2(101)$, (e) β - $\text{MnO}_2(110)$, (f) β - $\text{MnO}_2(211)$. The active site for intermediates adsorption during associative ORR highlighted by “*”. Mn and O are indicated blue and red, respectively.

The adsorption energy (E_{ads}) was calculated by

$$E_{\text{ads}} = E_{\text{complex}} - E_{\text{surface}} - E_{\text{adsorbate}} \quad (22)$$

where E_{complex} , E_{surface} , and $E_{\text{adsorbate}}$ represent the total energy of surface covered with adsorbate, the clean surface, and the isolated adsorbate, respectively. So, The E_{ads} of the intermediates (*OOH, *O, *OH) can be calculated by the following expression in eq. (23-26)

$$E_{\text{ads}}(*\text{OOH}) = E_{\text{DFT}}(*\text{OOH}) - E_{\text{DFT}}(*) - E_{\text{DFT}}(\text{OOH}) \quad (23)$$

$$E_{\text{ads}}(*\text{O}) = E_{\text{DFT}}(*\text{O}) - E_{\text{DFT}}(*) - \frac{1}{2}E_{\text{DFT}}(\text{O}_2) \quad (24)$$

$$E_{\text{ads}}(*\text{OH}) = E_{\text{DFT}}(*\text{OH}) - E_{\text{DFT}}(*) - E_{\text{DFT}}(\text{OH}^-) \quad (25)$$

The oxygen vacancy formation energy, $E_{\text{f}}(\text{O}_v)$, was defined as:

$$E_{\text{f}}(\text{O}_v) = E_{\text{O-vac}} - E_{\text{surface}} + \frac{1}{2}E_{\text{O}_2} \quad (26)$$

where $E_{\text{O-vac}}$ and E_{O_2} represent the energy of the surface with O_v site, and the isolated oxygen.

The Gibbs free energy (ΔG) was defined as the change in free energy of the system as it goes from initial state to final state and it is given by the following expression:

$$\Delta G = \Delta E + \text{ZPE} - T\Delta S + neU + \Delta G_{\text{pH}} \quad (27)$$

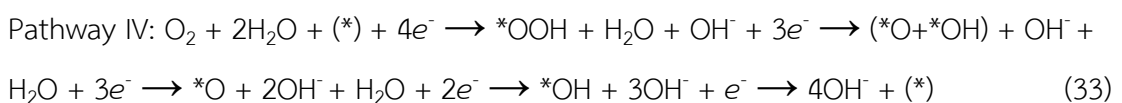
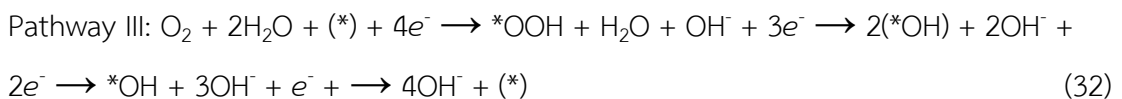
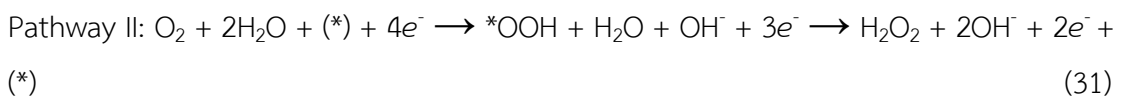
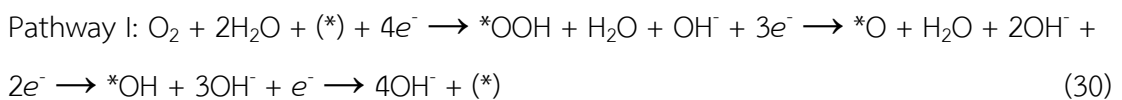
where ΔE is the difference of reaction energy between reactant and product molecules adsorbed on the surface. The zero-point energy (ZPE) is calculated from the vibrational frequencies of the adsorbed molecule, as above energies obtained from DFT calculations. T is the reaction temperature ΔS is the change of entropy energy. U and n are the electrode potential and pair of electron-proton each step, respectively. e is the electron. For term ΔG_{pH} is the effect of H^+ in electrolyte for calculating the effect of H^+ in DFT calculation.

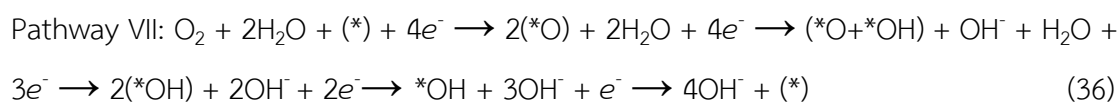
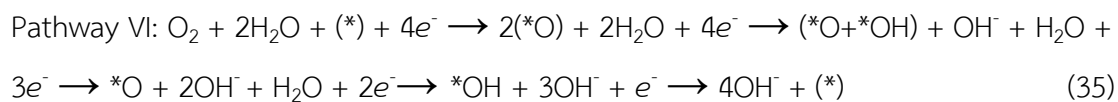
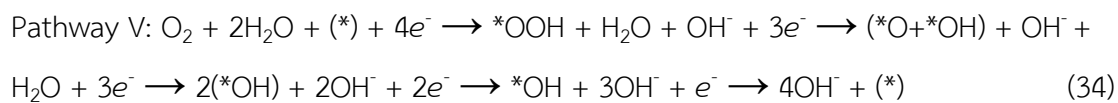
$$\text{ZPE} = \sum_i \left(\frac{1}{2} h\nu_i \right) \quad (28)$$

$$\Delta S = R \sum_i \left[\frac{h\nu_i}{k_{\text{B}}T \cdot \exp\left(\frac{h\nu_i}{k_{\text{B}}T}\right) - 1} - \ln \left(1 - \exp\left(\frac{-h\nu_i}{k_{\text{B}}T}\right) \right) \right] \quad (29)$$

where h , k_{B} , and R are the Planck, Boltzmann, and gas constant, respectively. ν_i is vibrational frequency of intermediate species

The possible ORR $4e^-$ and $2e^-$ pathways on the $\alpha\text{-MnO}_2$ and $\beta\text{-MnO}_2$, having 3 intermediates ($^*\text{O}$, $^*\text{OOH}$, $^*\text{OH}$), those adsorbed on Mn and O active sites as shown in eq. (30-36)





where (*) represents a clean surface. *OOH, *O, and *OH are intermediate species, which adsorb on a surface.



Chapter IV Results and Discussion

Density functional theory calculation is a useful method to study thermodynamics or energetic properties and the distribution of electron density. Hence, the following results are discussed of the properties of the system, which included structures, adsorption energies, Bader charge analysis, and Gibbs free energy diagrams. Finally, a description of the Gibbs free energy diagram on each mechanism are discussed in term of the limiting potential and overpotential on electrocatalytic reaction.

4.1 Intermediate adsorption on perfect surfaces

ORR has many intermediates: $^*\text{OOH}$, $^*\text{O}$, $^*\text{OH}$, 2^*O , $^*\text{O}+^*\text{OH}$, and 2^*OH due to many possible mechanisms. Optimized structures of intermediates adsorption on α - MnO_2 (110), α - MnO_2 (200), α - MnO_2 (211), β - MnO_2 (101), β - MnO_2 (110), and β - MnO_2 (211) are shown in Figure [21-26], respectively.

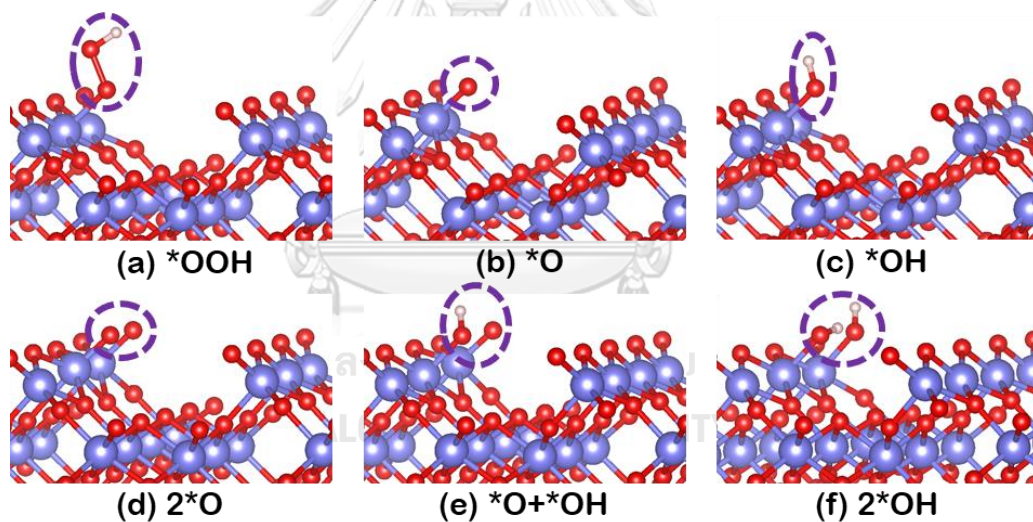


Figure 21 Optimized structure of intermediates adsorption for α - MnO_2 (110). Mn, O, and H indicated in blue, red, and white, respectively.

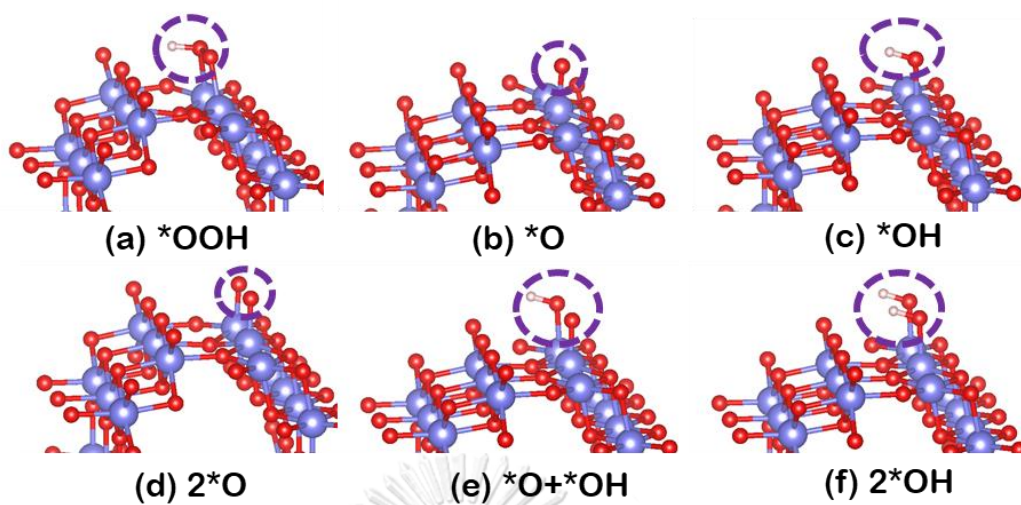


Figure 22 Optimized structure of intermediates adsorption for $\alpha\text{-MnO}_2$ (200). Mn, O, and H indicated in blue, red, and white, respectively.

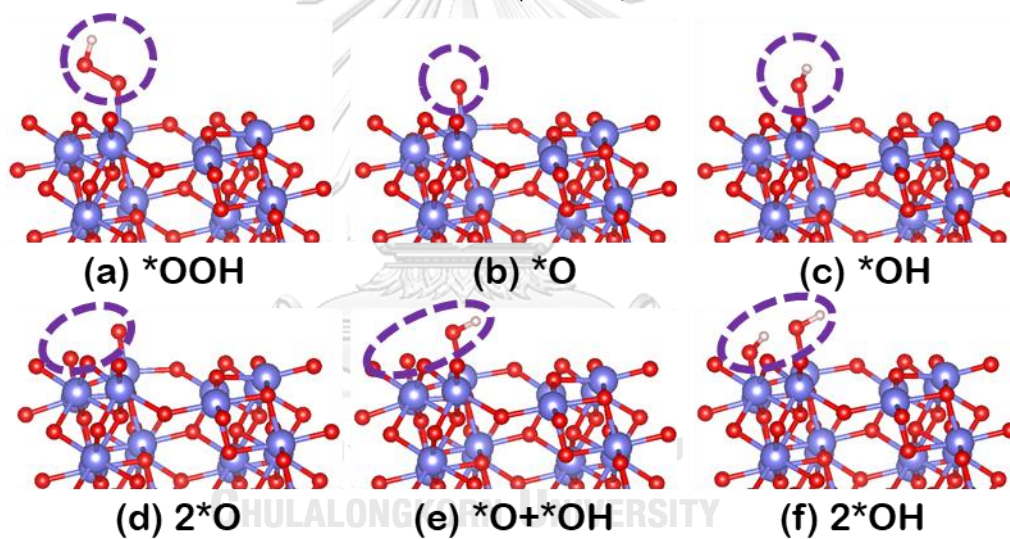


Figure 23 Optimized structure of intermediates adsorption for $\alpha\text{-MnO}_2$ (211). Mn, O, and H indicated in blue, red, and white, respectively.

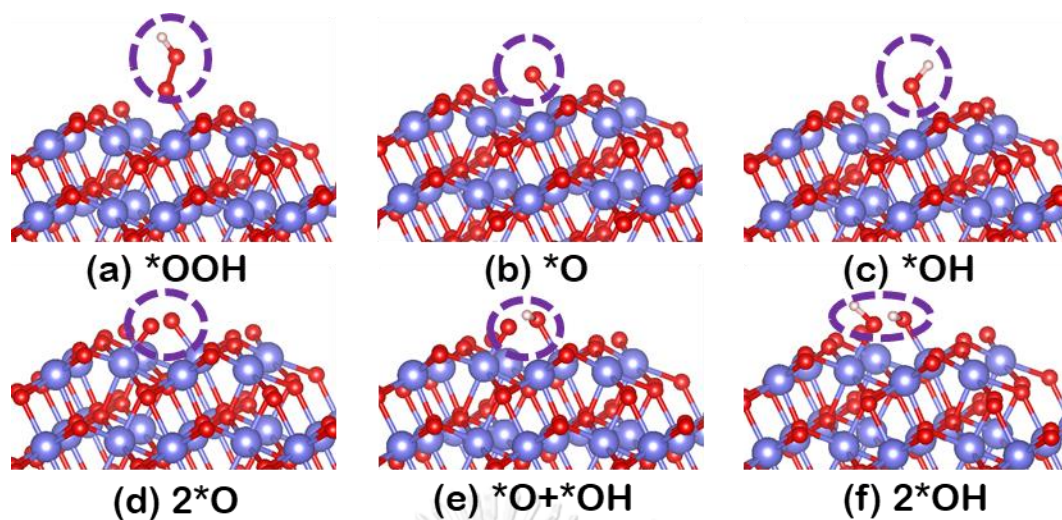


Figure 24 Optimized structure of intermediates adsorption for $\beta\text{-MnO}_2$ (101). Mn, O, and H indicated in blue, red, and white, respectively.

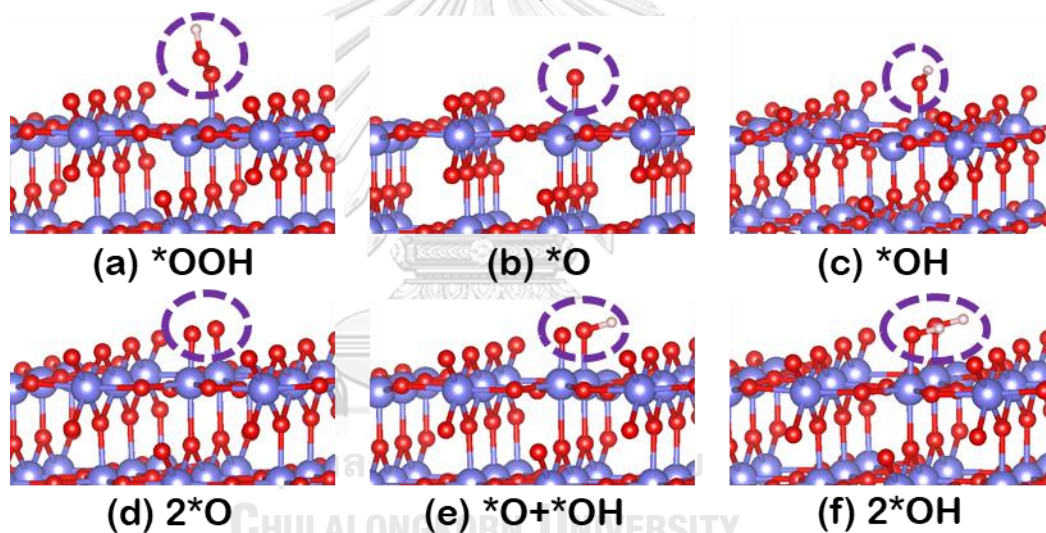


Figure 25 Optimized structure of intermediates adsorption for $\beta\text{-MnO}_2$ (110). Mn, O, and H indicated in blue, red, and white, respectively.

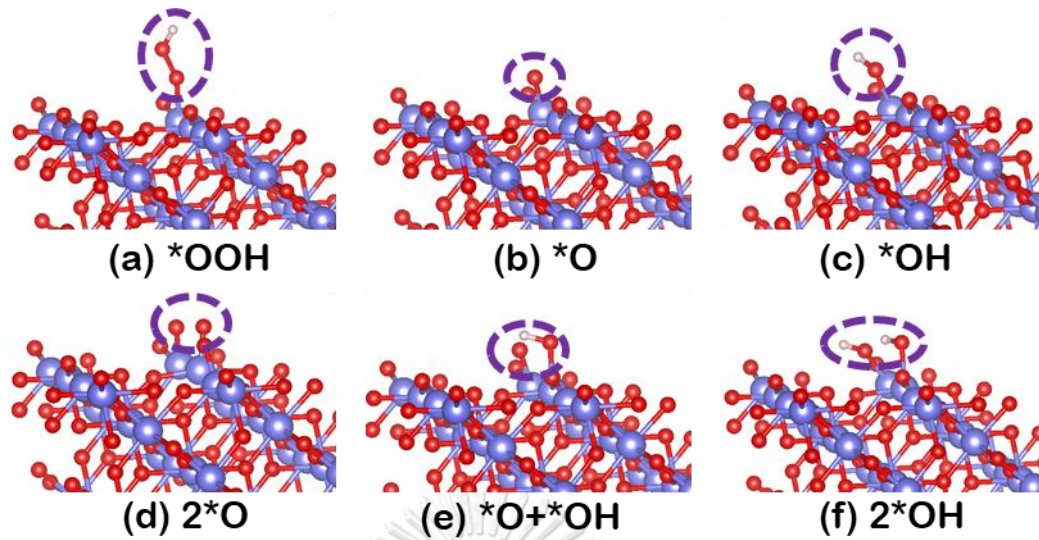


Figure 26 Optimized structure of intermediates adsorption for β -MnO₂ (211). Mn, O, and H indicated in blue, red, and white, respectively.

The adsorption energy (E_{ads}) of intermediates: *OOH, *O, *OH, 2*O, *O+*OH, 2*OH for perfect surfaces α -MnO₂(110), α -MnO₂(200), α -MnO₂(211), β -MnO₂(101), β -MnO₂(110), β -MnO₂(211) can be calculated in eq. (37-42). The adsorption energy is shown in Table 7.

$$E_{\text{ads}}(*\text{OOH}) = E_{\text{DFT}}(*\text{OOH}) - E_{\text{DFT}}(*) - E_{\text{DFT}}(\text{OOH}) \quad (37)$$

$$E_{\text{ads}}(*\text{O}) = E_{\text{DFT}}(*\text{O}) - E_{\text{DFT}}(*) - \frac{1}{2}E_{\text{DFT}}(\text{O}_2) \quad (38)$$

$$E_{\text{ads}}(*\text{OH}) = E_{\text{DFT}}(*\text{OH}) - E_{\text{DFT}}(*) - E_{\text{DFT}}(*\text{OH}) \quad (39)$$

$$E_{\text{ads}}(2*\text{O}) = E_{\text{DFT}}(2*\text{O}) - E_{\text{DFT}}(*) - 2E_{\text{DFT}}(\text{O}) \quad (40)$$

$$E_{\text{ads}}(*\text{O} + *\text{OH}) = E_{\text{DFT}}(*\text{O} + *\text{OH}) - E_{\text{DFT}}(*) - [E_{\text{DFT}}(\text{O}) + E_{\text{DFT}}(\text{OH})] \quad (41)$$

$$E_{\text{ads}}(2*\text{OH}) = E_{\text{DFT}}(2*\text{OH}) - E_{\text{DFT}}(*) - 2E_{\text{DFT}}(\text{OH}) \quad (42)$$

Table 7 Adsorption energy (in eV) of the intermediates: *OOH, *O, *OH, 2*O, *O+*OH, 2*OH for perfect surfaces.

	α -MnO ₂			β -MnO ₂		
	(110)	(200)	(211)	(101)	(110)	(211)
*OOH	-3.13	-3.95	-3.29	-3.19	-3.33	-2.53
*O	-2.53	-2.84	-2.73	-2.61	-2.21	-3.32
*OH	-1.97	-2.62	-2.22	-1.87	-2.41	-2.73
2*O	-4.95	-4.30	-5.70	-5.26	-4.75	-6.53
*O+*OH	-4.57	-5.34	-5.21	-4.75	-4.39	-5.33
2*OH	-4.12	-1.33	-4.82	-4.54	-4.01	-4.90

Bader charge analysis during ORR for perfect surfaces is shown in Table 8. The positive and negative values are electron depletion and electron accumulation, respectively. This result shows that the electron from the surfaces transferred to the intermediates (*OOH, *O, *OH, 2*O, *O+*OH, and 2*OH). The gaining of electron of single intermediate system (*OOH, *O, and *OH) is more than double intermediate system (2*O, *O+*OH, and 2*OH). The strain (in %) of the of the intermediates: *OOH, *O, *OH, 2*O, *O+*OH, 2*OH for perfect surfaces is shown in Table 9. The strain results for all intermediate on α -MnO₂(211) is lower than β -MnO₂(110), So the α -MnO₂(211) is easier reconstruct than β -MnO₂(110).

Table 8 Bader charge analysis (in $|e|$) of the intermediates: $^*\text{OOH}$, $^*\text{O}$, $^*\text{OH}$, 2^*O , $^*\text{O}+^*\text{OH}$, 2^*OH adsorbing on perfect surfaces.

	$\alpha\text{-MnO}_2$			$\beta\text{-MnO}_2$		
	(110)	(200)	(211)	(101)	(110)	(211)
$^*\text{OOH}$	+1.83	+1.81	+1.84	+1.86	+1.86	+1.80
$^*\text{O}$	+1.85	+1.86	+1.84	+1.87	+1.81	+1.84
$^*\text{OH}$	+1.85	+1.83	+1.85	+1.84	+1.86	+1.83
2^*O	+0.89	+0.82	+0.93	+0.91	+0.84	+1.01
$^*\text{O}+^*\text{OH}$	+0.76	+0.69	+0.83	+0.85	+0.66	+0.81
2^*OH	+0.65	+0.58	+0.75	+0.71	+0.54	+0.71

Table 9 Strain (in %) of the intermediates: $^*\text{OOH}$, $^*\text{O}$, $^*\text{OH}$, 2^*O , $^*\text{O}+^*\text{OH}$, 2^*OH for perfect surfaces.

	$\alpha\text{-MnO}_2$			$\beta\text{-MnO}_2$		
	(110)	(200)	(211)	(101)	(110)	(211)
$^*\text{OOH}$	1.99	1.08	1.39	1.06	2.16	1.75
$^*\text{O}$	8.00	3.27	4.11	3.74	8.24	1.77
$^*\text{OH}$	2.87	1.89	1.80	0.72	3.43	1.35
2^*O	5.77	2.76	3.78	3.48	5.46	2.25
$^*\text{O}+^*\text{OH}$	2.35	1.55	1.81	1.81	3.35	1.88
2^*OH	4.55	2.13	2.69	2.33	4.82	1.89

4.2 Intermediate adsorption on oxygen vacancy surfaces

Due to the experiment data revealing that the $\alpha\text{-MnO}_2(211)$ and $\beta\text{-MnO}_2(110)$ are the fresh and spent catalysts, respectively, the oxygen vacancy was studied on $\alpha\text{-MnO}_2(211)$ and $\beta\text{-MnO}_2(110)$. The oxygen vacancy sites were varied many positions of the top surface over $\alpha\text{-MnO}_2(211)$ and $\beta\text{-MnO}_2(110)$ to find the most stable $\text{O}_v\text{-MnO}_2$ surfaces, as shown in Figure 27. The $E_f(\text{O}_v)$ was calculated using eq.(25). The $E_f(\text{O}_v)$ of $\alpha\text{-MnO}_2(211)$ at the *1 and *2 are +1.61 eV and +3.16 eV, respectively. Hence, the $\text{O}_v\text{-}\alpha\text{-MnO}_2(211)$ at *1 position is more stable than that of *2 position because the $E_f(\text{O}_v)$

at *1 is lower than another position. For β -MnO₂(110), the $E_f(O_v)$ at *1 position is -0.14 eV while the $E_f(O_v)$ at *2 position is +3.40 eV. So, the O_v - β -MnO₂(110) at *1 position is more stable than *2 position. In addition, the O_v - β -MnO₂(110) is more stable than O_v - α -MnO₂(211) because the $E_f(O_v)$ of β -MnO₂(110) is much lower than the $E_f(O_v)$ of α -MnO₂(211).

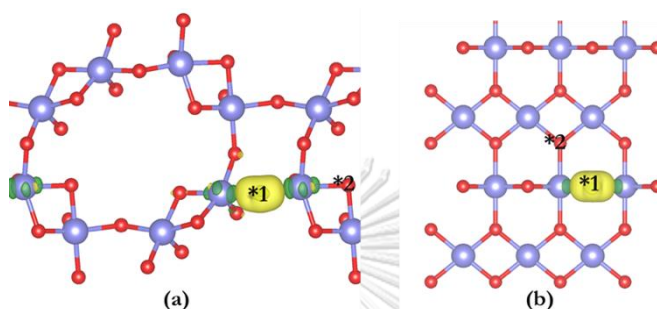


Figure 27 Top surface in terms of electron accumulation (yellow region) and electron depletion regions of (a) O_v - α -MnO₂(211) and (b) O_v - β -MnO₂(110), as isovalue ± 0.012 e/Å³. O_v positions were highlighted by *. Mn and O are indicated by blue and red, respectively.

Due to the preliminary result, the $4e^-$ ORR mechanism is studied only the mechanism in eq. (29). The optimized structures of intermediates adsorption on O_v - α -MnO₂ (211) and O_v - β -MnO₂(110) are shown in Figure 28. The adsorption energy of O_v -surfaces is illustrated in Table 10. The *OOH is the strongest chemisorption to all the O_v -surfaces, followed in order by *O and *OH, respectively. The Bader charge analysis of O_v -surfaces is shown in Table 11. The most gaining electrons is *O, followed in order by *OH and *OOH, respectively. The strain (in %) of the of the intermediates for O_v -surfaces is shown in Table 12. The *OOH is the most strain for O_v - α -MnO₂(211) and *O for O_v - β -MnO₂(110).

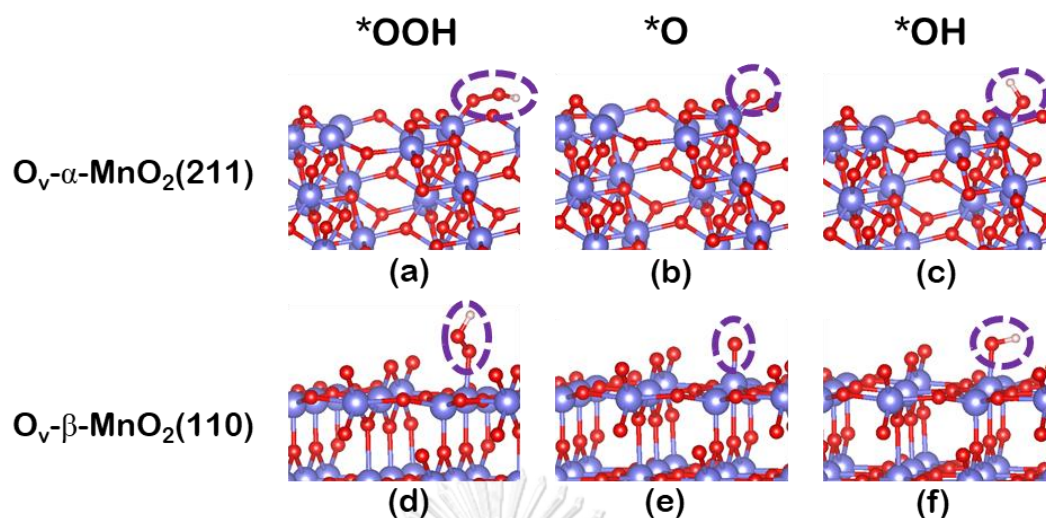


Figure 28 Optimized structure of intermediates adsorption (*OOH, *O, and *OH) for (a-c) $O_V\text{-}\alpha\text{-MnO}_2(211)$ and (d-f) $O_V\text{-}\beta\text{-MnO}_2(110)$. Mn, O, and H indicated in blue, red, and white, respectively.

Table 10 Adsorption energy (in eV) of the intermediates: *OOH, *O, *OH for oxygen vacancy surfaces.

	$O_V\text{-}\alpha\text{-MnO}_2(211)$	$O_V\text{-}\beta\text{-MnO}_2(110)$
*OOH	-3.46	-3.11
*O	-2.89	-2.18
*OH	-2.34	-1.98

Table 11 Bader charge analysis (in $|e|$) of the intermediates: *OOH, *O, *OH for oxygen vacancy surfaces.

	$O_V\text{-}\alpha\text{-MnO}_2(211)$	$O_V\text{-}\beta\text{-MnO}_2(110)$
*OOH	+0.24	+0.15
*O	+0.51	+0.41
*OH	+0.39	+0.30

Table 12 Strain (in %) of the intermediates: *OOH, *O, *OH for oxygen vacancy surfaces.

	$O_V\text{-}\alpha\text{-MnO}_2(211)$	$O_V\text{-}\beta\text{-MnO}_2(110)$
*OOH	5.68	1.88
*O	3.63	9.65
*OH	1.34	4.57

4.3 Intermediate adsorption on poisoning surfaces

Due to the preliminary result, the $4e^-$ ORR mechanism is studied only the mechanism in eq. (29). Optimized structures of intermediates adsorption on poisoning surfaces of both α - $\text{MnO}_2(211)$ and β - $\text{MnO}_2(110)$ have two $^*\text{OOH}$ as intermediate and ORR on poisoning surfaces are shown in Figure 29. The adsorption energy of poisoning surfaces is shown in Table 13. The $^*\text{OOH}$ exhibits the strongest chemisorption to all the poisoning surfaces, followed in order by $^*\text{O}$ and $^*\text{OH}$, respectively. The Bader charge analysis of poisoning surfaces is shown in Table 14. The most gaining electrons is $^*\text{O}$, followed in order by $^*\text{OH}$ and $^*\text{OOH}$, respectively. The strain (in %) of the of the intermediates for poisoning surfaces is shown in Table 15. The $^*\text{O}$ is the most strain for both poisoning- α - $\text{MnO}_2(211)$ and poisoning- β - $\text{MnO}_2(110)$.

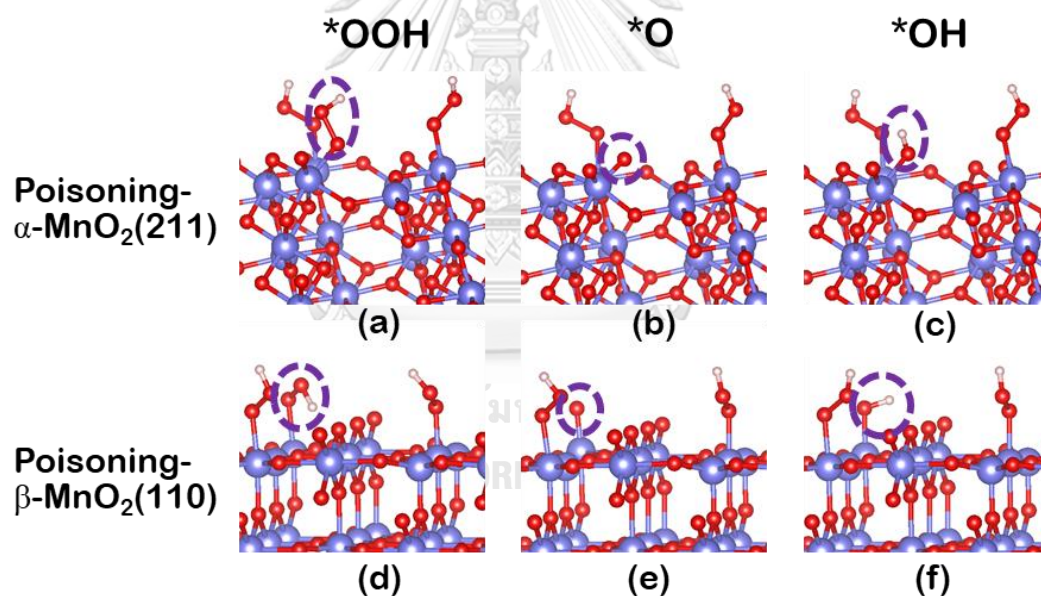


Figure 29 Optimized structure of intermediates adsorption ($^*\text{OOH}$, $^*\text{O}$, and $^*\text{OH}$) for (a-c) poisoning- α - $\text{MnO}_2(211)$ and (d-f) poisoning- β - $\text{MnO}_2(110)$. Mn, O, and H indicated in blue, red, and white, respectively.

Table 13 Adsorption energy (in eV) of the intermediates: *OOH, *O, *OH for poisoning surfaces.

	poisoning- α -MnO ₂ (211)	poisoning- β -MnO ₂ (110)
*OOH	-3.26	-3.22
*O	-2.85	-2.22
*OH	-2.19	-1.88

Table 14 Bader charge analysis (in |e|) of the intermediates: *OOH, *O, *OH for vacancy surfaces.

	poisoning- α -MnO ₂ (211)	poisoning- β -MnO ₂ (110)
*OOH	+0.22	0.00
*O	+0.47	+0.46
*OH	+0.38	+0.34

Table 15 Strain (in %) of the intermediates: *OOH, *O, *OH for vacancy surfaces.

	poisoning- α -MnO ₂ (211)	poisoning- β -MnO ₂ (110)
*OOH	1.17	1.47
*O	3.55	8.96
*OH	1.42	4.32

4.4 Gibbs free energy diagrams for oxygen reduction reaction

4.4.1 Spontaneous ORR

4.4.1.1 Four-electron pathway (pathway I)

Figure 30 shows the free energy diagram for the four-electron ORR of pathway I on various perfect surfaces. When the applied potential, U , is 0 V, all elementary steps are spontaneous. However, at the equilibrium, $U=1.23$ V, the reduction of O₂ to *OOH is nonspontaneous for all perfect surfaces and the reduction of *OOH to *O is nonspontaneous for α -MnO₂(110), α -MnO₂(200), α -MnO₂(211), β -MnO₂(101), and β -MnO₂(110). Limiting potential (blue line) defined as the maximum equilibrium potential made all elementary steps is spontaneous in relative free energy. Thus, the limiting potential (U_L) values are: 0.68 eV, 0.20 eV, 0.71 eV, 0.78 eV, 0.11 eV, and 0.15 eV for α -

MnO₂(110), α -MnO₂(200), α -MnO₂(211), β -MnO₂(101), β -MnO₂(110), and β -MnO₂(211), respectively.

The overpotential shows the performance of ORR in ZABs. It can be calculated in eq. (42)

$$\eta = 1.23 - \min(\Delta G_a, \Delta G_b, \Delta G_c, \dots) / e \quad (42)$$

The performance of ORR on various perfect surfaces for the four-electron ORR of pathway (I) is shown by value of limiting potential and overpotential in Table 15.

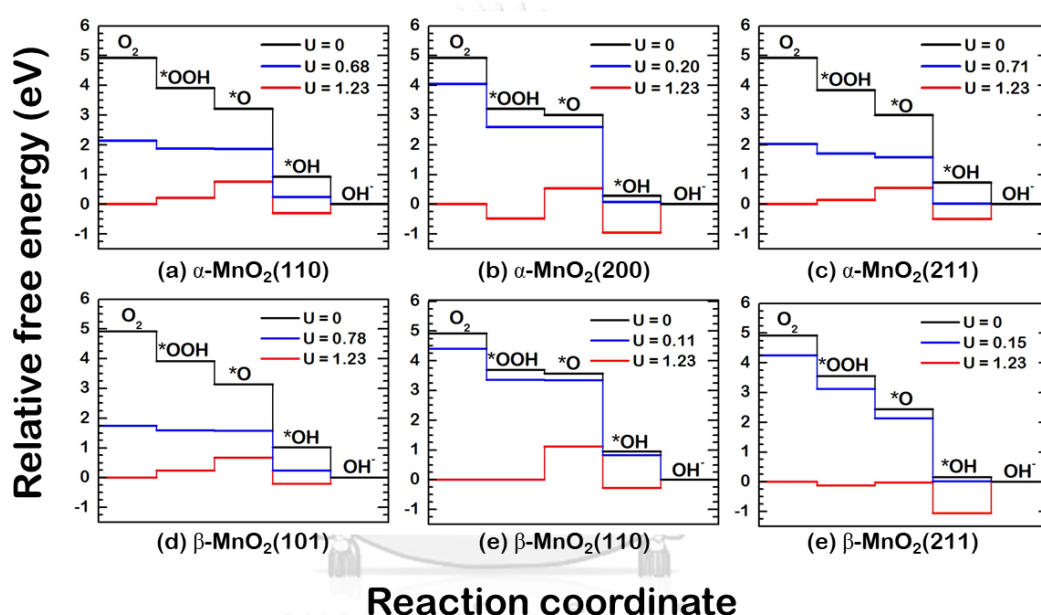


Figure 30 Relative free energy diagram for the four-electron associative ORR mechanism of pathway I on various perfect surfaces including of (a) α -MnO₂(100), (b) α -MnO₂(200), (c) α -MnO₂(211), (d) β -MnO₂(101), (e) β -MnO₂(110), and (f) β -MnO₂(211).

Figure 31 shows the free energy diagram for the four-electron ORR of pathway (I) on oxygen vacancy surfaces and poisoning surfaces. Their limiting potential and overpotential are shown in Table 15. The overpotential is decreased by O_v-surface and poisoning surface for β -MnO₂(110) referring to the O_v-surface and poisoning surface as the catalyst deactivation. For α -MnO₂(211), the overpotential of O_v surface is less than the perfect one. The ternary plots of the overpotential on 4e⁻ ORR for α -MnO₂(211) and β -MnO₂(110) are shown in Figure 32. The overpotential of α -MnO₂(211) is the orange and brown color while β -MnO₂(110) is the green color. This reveals that the

activity of α -MnO₂(211) is less than β -MnO₂(110). The O_v affected to decrease the overpotential for α -MnO₂(211) while the activity of O_v- β -MnO₂(110) is higher than on β -MnO₂(110) surface.

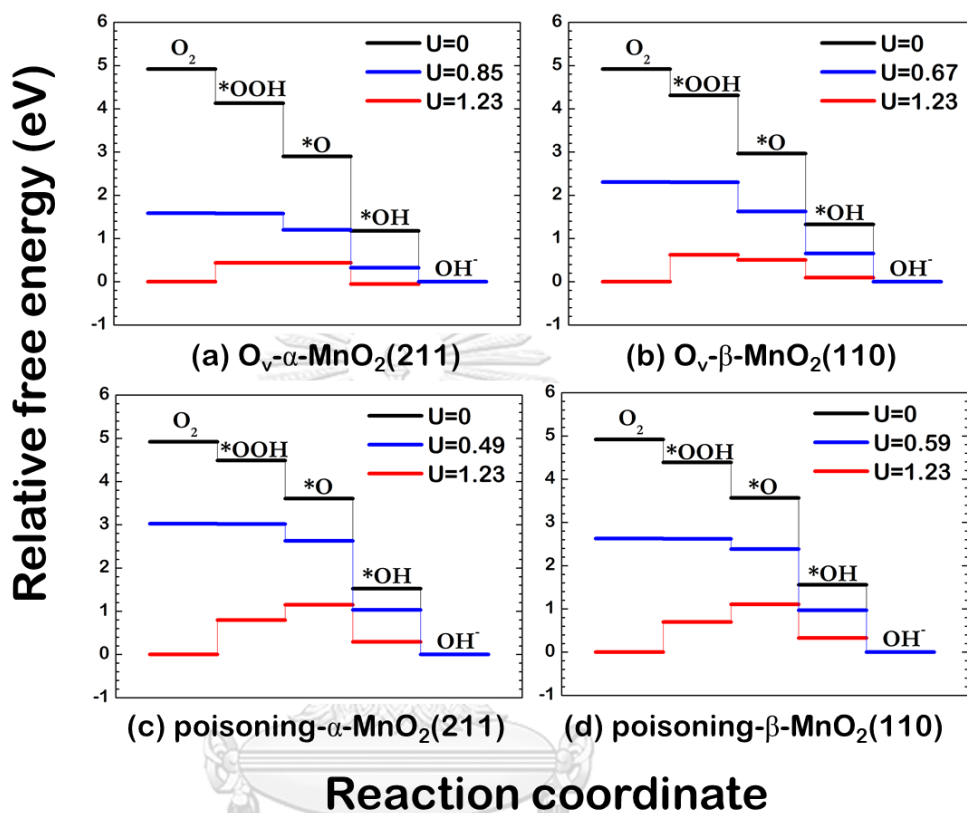


Figure 31 Relative free energy diagram for the four-electron associative ORR of pathway I on (a) O_v- α -MnO₂(211), (b) O_v- β -MnO₂(110), (c) poisoning- α -MnO₂(211), and (d) poisoning- β -MnO₂(110).

Table 15 Limiting potential (U_L) and overpotential (η) for the four-electron ORR of pathway I on perfect surfaces, oxygen vacancy surfaces, and poisoning surfaces

	Limiting potential (V)	Overpotential (V)
α -MnO ₂ (110)	0.68	0.54
α -MnO ₂ (200)	0.20	1.02
α -MnO ₂ (211)	0.71	0.40
β -MnO ₂ (101)	0.78	0.43
β -MnO ₂ (110)	0.11	1.10
β -MnO ₂ (211)	0.15	1.00
O _v - α -MnO ₂ (211)	0.85	0.44
O _v - β -MnO ₂ (110)	0.49	0.80
poisoning- α -MnO ₂ (211)	0.67	0.62
poisoning- β -MnO ₂ (110)	0.59	0.70

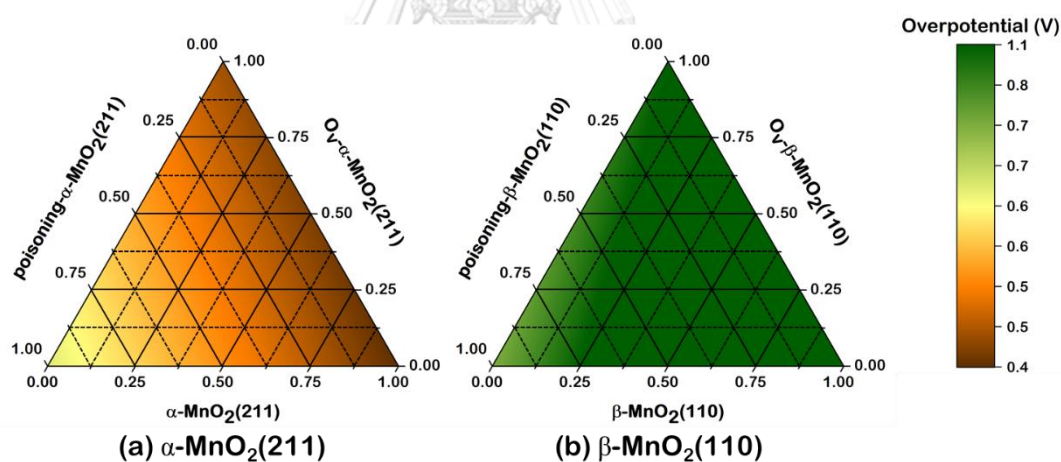


Figure 32 Ternary plots of the overpotential on 4e⁻ ORR pathway for (a) α -MnO₂(211) (b) β -MnO₂(101)

4.4.1.2 Two-electron pathway (pathway II)

Figure 33 shows the free energy diagram for the two-electron ORR of pathway II on perfect surfaces α -MnO₂(110), α -MnO₂(200), α -MnO₂(211), β -MnO₂(101), β -MnO₂(110), and β -MnO₂(211). Figure 34 shows the free energy diagram for the two-electron ORR of pathway (I) on oxygen vacancy surfaces and poisoning surfaces. Their limiting potential and overpotential is shown in Table 16. The overpotential is

decreased by O_v -surface and poisoning surface for β - $MnO_2(110)$ which refer to the O_v -surface and poisoning surface as the catalyst deactivation. The ternary plots of the overpotential on $2e^-$ ORR pathway for α - $MnO_2(211)$ and β - $MnO_2(110)$ are shown in Figure 35. The results show that the low activity found on the O_v surfaces and poisoning surfaces for both α - $MnO_2(211)$ and β - $MnO_2(110)$. In addition, the O_v and poisoning intermediates are the reason of catalyst deactivation.

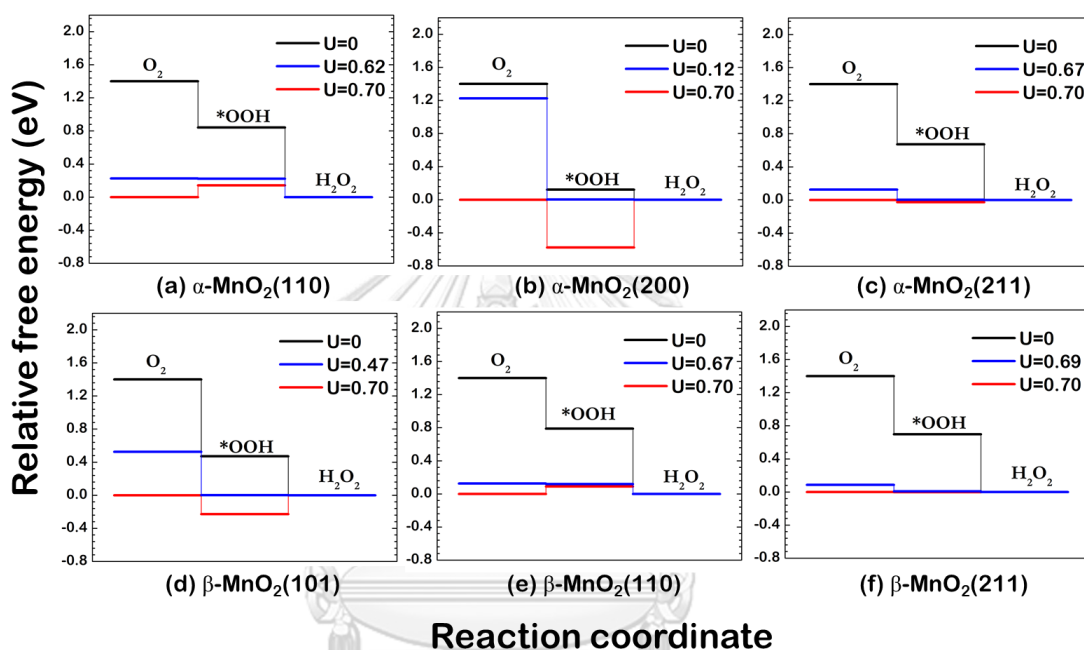


Figure 33 Relative free energy diagram for the two-electron associative mechanism ORR of pathway II on various perfect surfaces including of (a) α - $MnO_2(110)$, (b) α - $MnO_2(110)$, (c) α - $MnO_2(110)$, (d) β - $MnO_2(101)$, (e) β - $MnO_2(110)$, and (f) β - $MnO_2(211)$.

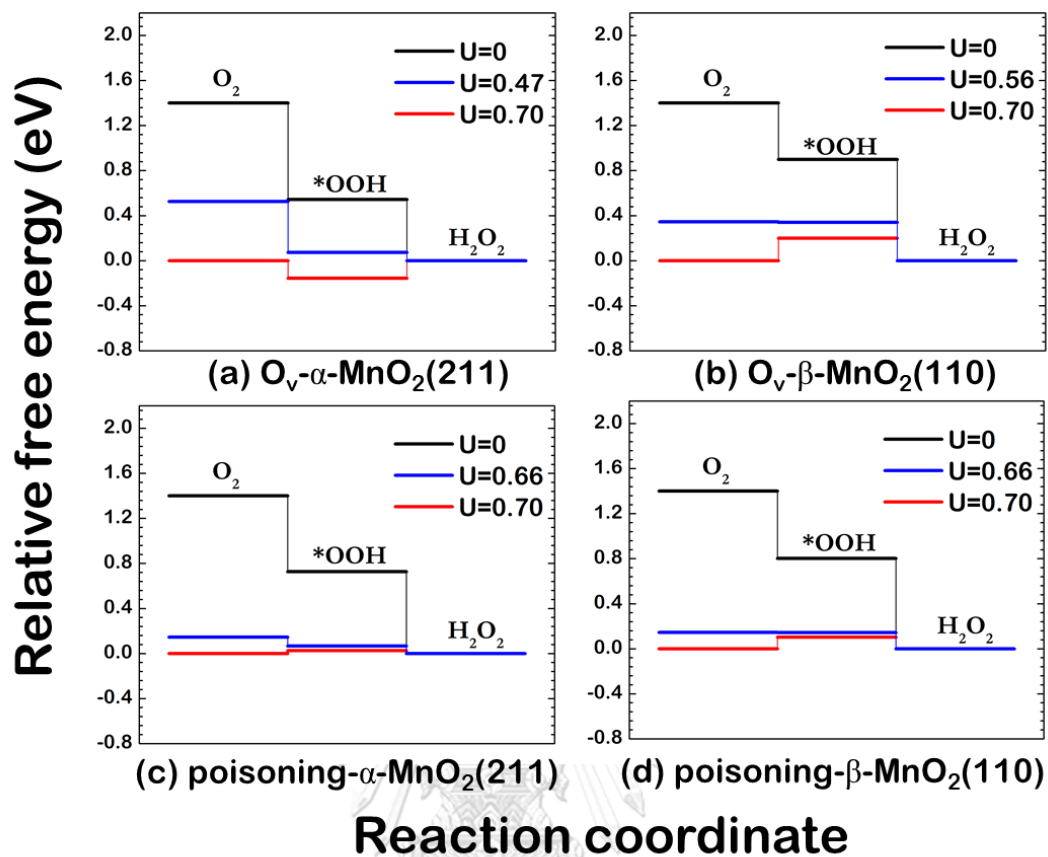


Figure 34 Relative free energy diagram for the two-electron associative ORR of pathway I on (a) $O_v-\alpha-MnO_2(211)$, (b) $O_v-\beta-MnO_2(110)$, (c) poisoning- $\alpha-MnO_2(211)$, and (d) poisoning- $\beta-MnO_2(110)$.

Table 16 Limiting potential (U_L) and overpotential (η) for the two-electron ORR of pathway I on perfect surfaces, oxygen vacancy surfaces, and poisoning surfaces.

	Limiting potential (V)	Overpotential (V)
α -MnO ₂ (110)	0.62	0.14
α -MnO ₂ (200)	0.12	0.58
α -MnO ₂ (211)	0.67	0.03
β -MnO ₂ (101)	0.67	0.09
β -MnO ₂ (110)	0.69	0.00
β -MnO ₂ (211)	0.47	0.23
O _v - α -MnO ₂ (211)	0.47	0.16
O _v - β -MnO ₂ (110)	0.56	0.20
poisoning- α -MnO ₂ (211)	0.66	0.03
poisoning- β -MnO ₂ (110)	0.66	0.10

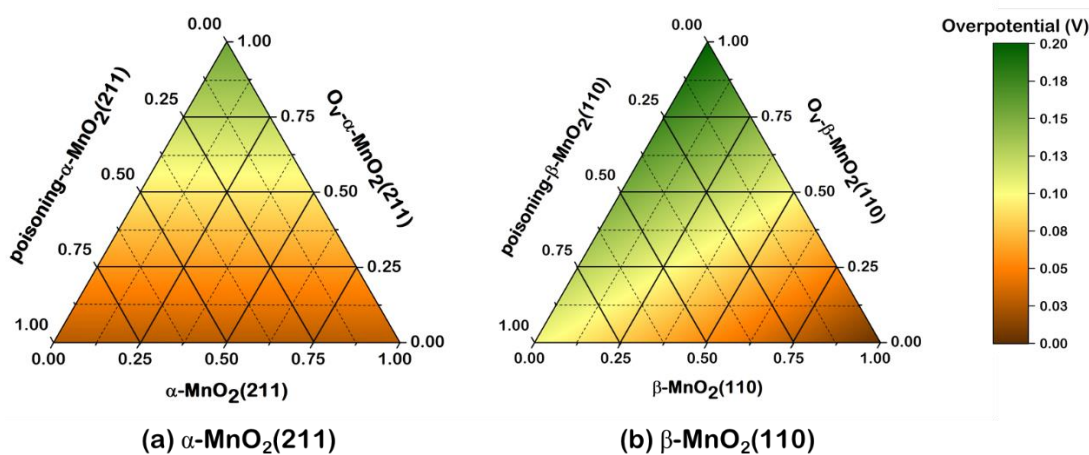


Figure 35 Ternary plots of the overpotential on $2e^-$ ORR pathway for (a) α -MnO₂(211) and (b) β -MnO₂(110).

4.4.2 nonspontaneous ORR (pathway III – VII)

Figure 36 shows nonspontaneous ORR for pathway III – VII on perfect surface α -MnO₂(211). The applied potential at $U=0$ V is used for this calculation. The pathway from III to VII is nonspontaneous. The reduction from $2(*OH)$ to $*OH$ are positive value for pathway III, V, and VII. While the reduction from $*OH$ to OH^- is positive value for all pathway (III – VII).

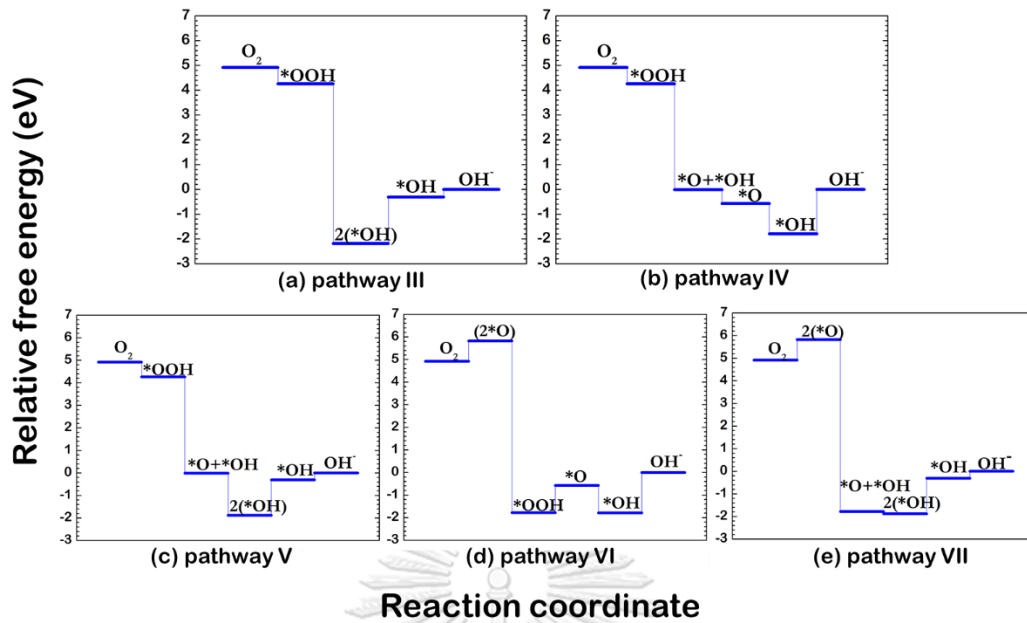


Figure 36 Nonspontaneous ORR for (a-e) pathway III – VII on perfect surface α - $\text{MnO}_2(211)$. The chemical potential $U = 0$ V.

Chapter V Conclusion

The deactivation of MnO₂ electrocatalyst in a ZAB was studied in term of phase transformation, oxygen vacancy surface, and poisoning surface via DFT calculation. The phase transformation from α -MnO₂(211) to β -MnO₂(110) on 4e⁻ ORR is clearly that the catalyst deactivation on MnO₂ because the limiting potential on α -MnO₂(211) is higher than the limiting potential on β -MnO₂(110). Moreover, the overpotential of β -MnO₂(110) is higher than α -MnO₂(211). For the 2e⁻ ORR, the catalytic activity of β -MnO₂(110) is better than α -MnO₂(211).

The O_v formation on β -MnO₂(110) is easier than α -MnO₂(211) because the O_v formation energy of β -MnO₂(110) is lower than α -MnO₂(211). The activity of O_v- β -MnO₂(110) is higher than β -MnO₂(110). So, the O_v improves the catalytic performance on β -MnO₂(110) for 4e⁻ ORR. The activity on α -MnO₂(211) is higher than O_v- α -MnO₂(211), which refer to the O_v is the catalyst deactivation for α -MnO₂(211). For the 2e⁻ ORR, the activity on O_v- α -MnO₂(211) is lower than α -MnO₂(211) while the O_v improves the catalytic performance on O_v- β -MnO₂(110).

The poisoning intermediate is *OOH in this work. For poisoning- α -MnO₂(211), the overpotential of poisoning surface is higher than α -MnO₂(211) for both 4e⁻ and 2e⁻ ORR which refers to the poisoning intermediate is the catalyst deactivation. For poisoning- β -MnO₂(110), the activity of poisoning- β -MnO₂(110) is higher than β -MnO₂(110) on 4e⁻ ORR while the activity of poisoning- β -MnO₂(110) is lower than β -MnO₂(110) on 2e⁻ ORR which refers to the poisoning intermediates is the catalyst deactivation on 2e⁻ ORR.

REFERENCES

- [1] Brown T, Borgia G, Sullivan J. *Nationalgeographic.org*.
<https://www.nationalgeographic.org/encyclopedia/renewable-resources/> [Accessed: 30 August 2021].
- [2] Nunez C. *Nationalgeographic.org*.
<https://www.nationalgeographic.com/environment/article/renewable-energy/>
 [Accessed: 30 August 2021].
- [3] Maclaurin G. *nrel.gov*. Available: http://www.nrel.gov/analysis/re_futures/.
 [Accessed: 30 August 2021].
- [4] Meylemans G. *eurobat.org*.
<https://www.eurobat.org/events/event/37-eurobat-battery-innovation-roadmap-2030-webinar> [Accessed: 30 August 2021].
- [5] Julien C, Massot M, Rangan S, Lemal M, Guyomard D. Study of structural defects in γ - MnO_2 by Raman spectroscopy. *J Raman Spectrosc*. 2002;33(4):223-228.
- [6] Hertzberg BJ, Huang A, Hsieh A, et al. Effect of Multiple Cation Electrolyte Mixtures on Rechargeable Zn- MnO_2 Alkaline Battery. *Chem Mater*. 2016;28(13):4536-4545.
- [7] Matsuki K and Kamada H. OXYGEN REDUCTION ELEC, I ROCATALYSIS ON SOME MANGANESE OXIDES. *Electrochim Acta*. 2020;31(1):13-18
- [8] Meng Y, Song W, Huang H, Ren Z, Chen SY, Suib SL. Structure-property relationship of bifunctional MnO_2 nanostructures: Highly efficient, ultra-stable electrochemical water oxidation and oxygen reduction reaction catalysts identified in alkaline media. *J Am Chem Soc*. 2014;136(32):11452-11464.
- [9] Gu Y, Yan G, Lian Y, et al. Mn III -enriched α - MnO_2 nanowires as efficient bifunctional oxygen catalysts for rechargeable Zn-air batteries. *Energy Storage Materials*. 2019;23(5):252-260.
- [10] Xu N, Nie Q, Luo L, et al. Controllable Hortensia-like MnO_2 Synergized with Carbon Nanotubes as an Efficient Electrocatalyst for Long-Term Metal-Air Batteries. *ACS Appl Mater Interfaces*. 2019;11(1):578-587.
- [11] Selvakumar K, Senthil Kumar SM, Thangamuthu R, et al. Physiochemical investigation of shape-designed MnO_2 nanostructures and their influence on oxygen

reduction reaction activity in alkaline solution. *J Phys Chem C*. 2015;119(12):6604-6618.

[12] Cheng F, Zhang T, Zhang Y, Du J, Han X, Chen J. Enhancing Electrocatalytic Oxygen Reduction on MnO₂ with Vacancies**. *Angew Chem Int. Ed*. 2013:2474-2477.

[13] Ren S, Duan X, Liang S, Zhang M, Zheng H. Bifunctional electrocatalysts for Zn-air batteries: Recent developments and future perspectives. *J Mater Chem A*. 2020;8(13):6144-6182.

[14] 2021. Available: <https://pv-magazine-usa.com/2020/01/27/zinc-air-battery-being-deployed-in-new-york-aims-for-extremely-low-45-kwh-cost/> [Accessed: 1 February 2021].

[15] Kim JH, Kim YT, Joo SH. Electrocatalyst design for promoting two-electron oxygen reduction reaction: Isolation of active site atoms. *Curr Opin Electrochem*. 2020;21:109-116.

[16] Li L, Feng X, Nie Y, et al. Insight into the Effect of Oxygen Vacancy Concentration on the Catalytic Performance of MnO₂. *ACS Catal*. 2015;5(8):4825-4832.

[17] Shin J, Seo JK, Yaylian R, Huang A, Meng YS. A review on mechanistic understanding of MnO₂ in aqueous electrolyte for electrical energy storage systems. *Int Mater Rev*. 2020;65(6):356-387.

[18] Tompsett DA, Parker SC, Islam MS. Surface properties of α -MnO₂: relevance to catalytic and supercapacitor behaviour†. *J Mater Chem*. 2014:15509-15518.

[19] Tompsett DA, Parker SC, Islam MS. Rutile (β -)MnO₂ surfaces and vacancy formation for high electrochemical and catalytic performance. *J Am Chem Soc*. 2014;136(4):1418-1426.

[20] Chombo PV, Laonual Y. A review of safety strategies of a Li-ion battery. *J Power Sources*. 2020;478(7):228649.

[21] Kulkarni A, Siahrostami S, Patel A, Nørskov JK. Understanding Catalytic Activity Trends in the Oxygen Reduction Reaction. *Chem Rev*. 2018;118(5):2302-2312.

[22] Zhang X, Yang Z, Lu Z, Wang W. Bifunctional CoNx embedded graphene electrocatalysts for OER and ORR: A theoretical evaluation. *Carbon N Y*. 2018;130:112-119.

- [23] Mellan TA, Maenetja KP, Ngoepe PE, Woodley SM, Catlow CRA, Grau-Crespo R. Lithium and oxygen adsorption at the β -MnO₂ (110) surface. *J Mater Chem A*. 2013;1(47):14879-14887.
- [24] Kresse G, Hafner J. Ab initio molecular dynamics for liquid metals. *Phys Rev B*. 1993;47(1):558.
- [25] Kresse G, Hafner J. Ab initio molecular-dynamics simulation of the liquid-metal–amorphous-semiconductor transition in germanium. *Phys Rev B*. 1994;49(20):14251.
- [26] Kresse G, Furthmüller J. Efficiency of ab-initio total energy calculations for metals and semiconductors using a plane-wave basis set. *Comput Mater Sci*. 1996.;6(1):15-50.
- [27] Kresse G, Furthmüller J. Efficient iterative schemes for ab initio total-energy calculations using a plane-wave basis set. *Phys Rev B*. 1996; 54(16):11169.
- [28] Perdew, J.P., Burke K, Ernzerhof M. Generalized gradient approximation made simple. *Phys Rev Lett*. 1996;77(18):3865.
- [29] Crespo Y, Seriani N. A lithium peroxide precursor on the α -MnO₂(100) surface. *J Mater Chem A*. 2014:16538-16546.
- [30] Chen Z, Li G, Zheng H, Shu X, Zou J, Peng P. Applied Surface Science Mechanism of surface effect and selective catalytic performance of MnO₂ nanorod: DFT + U study. *Appl Surf Sci*. 2017;420:205-213.
- [31] Stefan G, Jens A, Stephan E, Helge K. A consistent and accurate ab initio parametrization of density functional dispersion correction (DFT-D) for the 94 elements H-Pu. *J Chem Phys*. 2010;132(15):154104.
- [32] Persson K. *Materials Project*. <https://materialsproject.org/materials/mp-19395/>. [Accessed: 1 November 2020].
- [33] Persson K. *Materials Project*. <https://materialsproject.org/materials/mp-510408/>. [Accessed: 1 November 2020].



จุฬาลงกรณ์มหาวิทยาลัย
CHULALONGKORN UNIVERSITY

REFERENCES



จุฬาลงกรณ์มหาวิทยาลัย
CHULALONGKORN UNIVERSITY



จุฬาลงกรณ์มหาวิทยาลัย
CHULALONGKORN UNIVERSITY

VITA

NAME	Puwit Buapin
DATE OF BIRTH	13 Nov 1996
PLACE OF BIRTH	Phatthalung, Thailand
INSTITUTIONS ATTENDED	B.Sc.(Chemical engineering) Chulalongkorn University
HOME ADDRESS	62/1435 Aspire Erawan building, Sukhumvit rd., Pak nam, Mueng Samutprakan, Samutprakan Thailand
AWARD RECEIVED	Best presentation award at the 30th Thai Institute of Chemical Engineering and Applied Chemistry Conference

